The University of Manchester
School of Physics and Astronomy

Substructures in galaxy clusters

Observability study using the MACSIS hydrodynamical simulation and Sunyaev-Zel'dovich signals

Edoardo Altamura*

PHYS 40182
MPhys Thesis

Supervisor: Dr. Scott Kay
Project collaborator: Martin Murin

May 13, 2019

Abstract

The Λ-Cold Dark Matter model predicts that large galaxy clusters should retain a complex and dynamic substructure, characterising both the dark matter distribution as well as their baryonic component. The hot ionised gas, shock-heated by the clusters' deep gravitational potential, is known to comptonise the photons from the Cosmic Microwave Background, giving rise to the thermal (tSZ) and kinetic (kSZ) Sunyaev-Zel'dovich effects. In this study, the MAssive ClusterS and Intercluster Structures (MACSIS) hydrodynamical simulation provided a sample of 390 clusters with total masses between $10^{15} - 10^{16} M_\odot$, which constitute an exceptional probe for the dynamics of substructures using kSZ information. The hot gas bound to substructures was analysed using the outputs form the `SUBFIND` code and the results from a pipeline dedicated to the reconstruction/analysis of galaxy cluster kSZ maps. The combination of these two independent methods allowed the computation of the fraction of `SUBFIND` substructures that were detected by the pipeline algorithms. This analysis showed that the substructures orbiting the main cluster within its virial radius can be detected with a probability 8 times smaller than substructures outside the virial region. Substructures with mass $M \gtrsim 10^{13} M_\odot$ and modest line of sight velocity were found to deliver a $\approx 20\%$ detectability rate, in contrast with predictions from the kSZ theory. Such phenomenon is attributed to a high-mass bias introduced by the fluctuation detection algorithm, although its origin has not yet been uniquely identified. The relevance of this work for kSZ observations involves predictions for the observability of substructures in large galaxy clusters, the reconstruction of their kinematics and also the assessment of the statistical significance associated with their detection.

Key words: clusters of galaxies: substructures · hydrodynamical simulation · Sunyaev-Zel'dovich effects

*E-mail: edoardo.altamura@student.manchester.ac.uk

1 Introduction

Amongst the largest self-gravitating systems in the Universe, galaxy clusters are the subjects of extremely active areas of research in Astrophysics and Cosmology. Their study has been crucially important in the construction of the Λ-Cold Dark Matter (ΛCDM) model, which describes the evolution of the Universe from the post-recombination epochs to the present day (West et al., 1995; Diaferio et al., 2008; Allen et al., 2011; Kravtsov & Borgani, 2012; Weinberg et al., 2013; Conselice et al., 2014; Tweed et al., 2018; Perrott et al., 2019). The ΛCDM theory predicts that small gravitating systems form at early times in the matter-dominated era. They subsequently interact with the surrounding material and then merge into larger galaxy clusters, which are likely to exhibit ongoing merging and complex dynamics even at the present day (Press & Schechter, 1974; Geller & Beers, 1982; Blumenthal et al., 1984; Binney & Tremaine, 1987; White & Frenk, 1991; Kauffmann & White, 1993; West et al., 1995; Cole et al., 2000; Diaferio et al., 2008; Allen et al., 2011; Walker et al., 2019b).

This result, encoding the concept of *hierarchical structure formation*, implies that smaller and older galaxy clusters are expected to show a low degree of internal substructure, in contrast with larger and younger systems, whose morphology and thermodynamics can be highly dominated by merging phenomena. The modern picture of a large galaxy cluster therefore consists in a central halo, generally located at a node of the cosmic web, connected to neighbouring filaments and sheets. The central halo gives rise to a deep gravitational potential well, which can host more than 10^3 galaxies, dark matter and diffuse ionised hot gas, defined as Intra-Cluster Medium (ICM). Within a distance of ~ 10 Mpc from the richest cluster, the baryons and dark matter are gravitationally attracted along the filaments (or sheets) towards the central potential, originating a flow of infalling smaller halos. Once captured, these subhalos continue orbiting the primary cluster and form its substructure (Geller & Beers, 1982; Dressler & Shectman, 1988; Lacey & Cole, 1993; West et al., 1995; Allen et al., 2011; Walker et al., 2019b; Nagai & Lau, 2011).

Similarly to galaxy clusters, subhalos are self-bound objects, populated by $\sim 10 - 100$ galaxies, dark matter and hot gas. Given their lower mass, the majority of them must have formed at early times, before merging into larger systems. Over the last few billions of years in the cosmic history, a galaxy cluster is expected to have merged with several subhalos, developing an anisotropic structure which retains the thermodynamic and kinematic information of the older objects (Geller & Beers, 1982; Dressler & Shectman, 1988; West et al., 1995; Nagai & Lau, 2011).

Over the last three decades, high resolution cosmological simulations have played a crucial role in the study of galaxy clusters: they allowed the interpretation of early observations (e.g. Byram et al. 1966; Raymond & Smith 1977; Zwicky 1951) through the theoretical framework of the extended Press & Schechter (1974) theory, (see also Bond et al. 1991 and Bower 1991). Furthermore, numerical $\mathcal{N}$-body simulations have indeed confirmed that less-virialised large galaxy clusters are expected to show a high degree of substructure, deriving from active cluster mergers (Moore et al., 1999; Ghigna et al., 2000; Springel et al., 2001b; De Lucia et al., 2004; Gao et al., 2004; Kravtsov et al., 2004; Diemand et al., 2004). These studies have implemented Dark Matter Only (DMO) simulations and they traced the evolution of mass tracers under the sole effect of gravity.

As noted in Dolag et al. (2009), $\mathcal{N}$-body models can provide useful insight into the formation of dark matter halos in a ΛCDM Universe, but they lack in accuracy and predictive power when analysing the effects of baryonic physics. McCarthy et al. (2008) have suggested, among others, that the collisional nature of the hot gas is often crucial for studying the interaction between subhalos and the ICM. For instance, several analyses have suggested that the ionised gas bound to subhalos can be subject to a severe stripping due to ram pressure when entering the hot gas of the primary cluster, leaving the compact stellar core and collisionless dark matter halo exposed to the ICM (Gill et al., 2005; Takizawa, 2005; Tonnesen & Bryan, 2008; Bahé et al., 2012; Altamura, 2019; Murin, 2019). In order to model the effects of baryons, many recent high-resolution simulations have been deployed in two versions: the DMO run, as discussed before, and the hydrodynamical (abbreviated as HYDRO) simulation, which combines collisional astrophysical processed and gravity.

The cosmological simulation examined in the present study has been developed by Barnes et al. (2015, 2017) using the `Gadget-3` code (Springel et al., 2001a; Springel, 2005). This project, known as MAssive ClusterS and Intercluster Structures (MACSIS), includes a sample of 390 simulated galaxy clusters, having masses approaching $10^{16} M_\odot$ and modelled using gravity and hydrodynamical models (see Barnes et al. 2015, 2017; Altamura 2019; Murin 2019 and references therein for a detailed description). Within the ΛCDM scenario, galaxy clusters analogous to those in the MACSIS catalogue must have formed at very late times. Their history must therefore be characterised by numerous merging events, which have originated a rich substructure, ideal for the study of subhalos within galaxy clusters.

Previous works (Henson et al., 2017; Altamura, 2019; Murin, 2019) have analysed the effects of baryons in the dark matter field of the MACSIS clusters, revealing that radiative cooling is the most likely factor enhancing the formation of small-scale ($10^{11} - 10^{12} M_\odot$) and high-concentration subhalos, as compared to the DMO simulation. Furthermore, these analyses have shown very few subhalos, with masses between $10^{11} - 10^{13} M_\odot$, exhibiting little to no self-bound gas. Such a low gas content is re-examined in the present work and combined with the thermodynamics and kinematics of the subhalos, with the aim of mapping the distribution of their hot gas and guiding the interpretation of mock observations of galaxy clusters.

The observational research on galaxy clusters has been developed on various fronts, all relying on multi-wavelength studies. Each one of these is best calibrated for exploiting different physical effects, in order to retrieve specific physical quantities (e.g. mass M or temperature T of the hot gas), or combinations of them (e.g. the mass-weighted temperature $M \cdot T$) (Diaferio et al., 2008; Allen et al., 2011; Mroczkowski et al., 2019; Walker et al., 2019b,a). Among the most studied phenomena occurring in galaxy clusters are the bremsstrahlung emission, responsible for

the X-ray radiation generated by the electrons in the diffuse ionised hot ICM (e.g. Allen et al. 2011), and the Sunyaev-Zel'dovich (SZ) effects, which causes the Cosmic Microwave Background (CMB) to appear hotter or cooler than average along the line of site of the hot gas (Zeldovich & Sunyaev, 1969; Sunyaev & Zeldovich, 1969, 1970a,b,c, 1972).

The SZ effect originates from the Compton scattering of CMB photons off free electrons in the ionised hot gas of galaxy clusters. According to the frequency ν of observation, the CMB spectrum will appear colder for $\nu \lesssim 220$ GHz and hotter for $\nu \gtrsim 220$ GHz, in correspondence of hot gas clouds. For this reason, the SZ effect is considered a spectral distortion of the CMB, away from the approximately perfect black-body profile (Zeldovich & Sunyaev, 1969; Sunyaev & Zeldovich, 1969; Walker et al., 2019b; Mroczkowski et al., 2019). The macroscopic phenomenology of the SZ effect depends upon the velocity distribution of the electron gas in the cloud, broadly defined as the hot Inter-Galactic Medium (IGM). The Compton effect, calculated for isotropic plasma with a relativistic Maxwell-Boltzmann velocity distribution, yields the *thermal* Sunyaev-Zel'dovich (tSZ) effect, which results in the first-order distortion described above. However, the bulk motion of the cloud along the line of sight may contribute to an additional component in the electron velocity, which can be measured as a second-order spectral distortion, known as *kinematic* Sunyaev-Zel'dovich (kSZ) effect (see Birkinshaw 1999; Carlstrom et al. 2002; Mroczkowski et al. 2019 for full reviews).

The predictions advanced by Zeldovich & Sunyaev (1969) have been first confirmed by single-dish (Pariiskii, 1973; Birkinshaw et al., 1978) and interferometric observations (Moffet & Birkinshaw, 1989; Jones et al., 1993; Grainge et al., 1993; Carlstrom et al., 1996), with the detection of a significant decrement in surface brightness in radio bands ($15 - 90$ GHz). These results, compliant with the characteristic spectral signature of the tSZ effect, opened the way to extensive surveys, aimed at conveying SZ measurements from numerous galaxy clusters and achieving over the last decade increasingly better spectral coverage, angular resolution and surface brightness sensitivity (e.g. Zemcov et al. 2010; Mason et al. 2010; Planck Collaboration et al. 2016a,b; Mroczkowski et al. 2019; Basu et al. 2019). Very recently, the advent of highly coherent interferometers and low-noise Kinetic Inductance Detectors (KIDs) provided the necessary technology not only for studying the global IGM and ICM properties of galaxy clusters, but also their substructure (Adam et al., 2014, 2016; Basu et al., 2016, 2019).

The tSZ effect is expected to introduce a deviation $\sim 10^4$ times smaller than the amplitude of the CMB spectrum, while the kSZ spectral distortion for a subhalo moving at 10^3 km s^{-1} along the line of sight can be up to one order of magnitude smaller than the tSZ signal (Mroczkowski et al., 2019). This factors explain the relatively late pioneering detection of the kSZ effect on the multiple merger MACS J0717.5+3745, presented in Mroczkowski et al. (2012) and confirmed in Sayers et al. (2013). Building upon such result, the Institut de Radio Astronomie Millimétrique (IRAM) commissioned the New IRAM Kids Array (NIKA) cameras, equipped with new generation KIDs

and optimised for kSZ observations of small-scale substructures in galaxy clusters (e.g. Adam et al. 2017).

The present work was largely motivated and inspired by the recent advancements owed to the NIKA Collaboration, in particular the new kinematic study on MACS J0717.5+3745 presented by Adam et al. (2017). The velocity field of the some of the main substructures in this galaxy cluster have been detected with likelihood up to 5.1σ, consistent with previous independent observations (Sarazin, 2002; Ma et al., 2009; Limousin et al., 2012; Sayers et al., 2013; Limousin et al., 2016). However, Adam et al. (2017) have revealed the dependence of the kSZ peak likelihood upon the modelling pipeline, which maximally affects detections of $1-2\sigma$. Our results from the MACSIS simulation aim at guiding the construction of reliable models of upcoming kSZ observations and interpreting the dynamics of subhalos in large merger systems (see also Jauzac et al. 2018).

The present work is divided in five sections, each illustrating a specific aspect of the project. Section 2 includes a brief description of the MACSIS simulations, following Barnes et al. (2017); Altamura (2019); Murin (2019), together with details about the astrophysics of the SZ effects. The main results from the simulation are presented in the following three parts: section 3 analyses the thermodynamic properties of the hot ionised gas and defines the context for the construction of mock tSZ and kSZ maps. Section 4 describes a prescription for the computation of SZ signals on the MACSIS dataset and illustrates the algorithm for the detection of fluctuations in simulated maps. Section 5 conveys the results from previous sections into substructure catalogues, which are the basis for stating conclusions on the detection probabilities of SZ fluctuations. Lastly, section 6 contains the summary and discussion of the results and concludes this scientific report with a perspective on future work.

2   Theory and methodology

This section includes three main parts. The first one illustrates the formation, evolution and the general properties of galaxy clusters and subhalos. The second part includes a description of the MACSIS hydrodynamical simulation and the pipeline used to extract the data used in this study. The last part introduces the SZ effects, the physical process involved, the observational challenges related to their detection and their relevance for galaxy cluster astrophysics.

2.1   Formation and general properties of galaxy clusters

The mass of large galaxy clusters is dominated by dark matter halos, while the baryonic component (e.g. stars and gas) is expected to trace the dark matter distribution (Arons & Silk, 1968; Binney & Tremaine, 1987; Gnedin & Hui, 1998). The simplest model able to describe the formation of such halos is known as the *spherical top-hat collapse* (STHC) model.
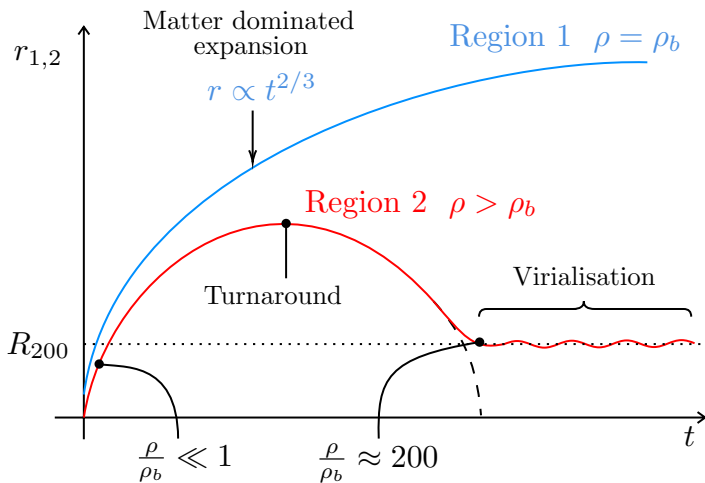
Figure 1: This plot shows schematically the time-evolution of the physical radii of the two regions of space considered in the STHC model. The blue line indicates the expansion of region 1, following the expansion law of a matter dominated Universe (i.e. Einstein-de Sitter), while the red line displays the effect of the overdense region 2. The dashed black line marks the prediction of the STHC model, while red solid line above it represents the more realistic scenario of the virialised dark matter halo. Lastly, R_{200} bounds the region where $\rho \gtrsim 200 \ \rho_b$, containing the matter affected by the collapse. Image created using PGF/Ti*kz* modules.

Let us consider two disconnected spherical regions of the Universe, permeated with an isotropic dark matter field having density ρ_b. This field constitutes the dark matter *background*. The first spherical region, having physical (i.e. non-comoving) radius r_1 and mass M_1, is characterised by a constant density $\rho_1 = \rho_b$. The second region is defined to have mass $M_2 = M_1$ and density $\rho_2 = \rho > \rho_b$, indicating that it is overdense. By applying Newton's laws, one can obtain the differential equation for the radii r_1 and r_2 of the regions:

$$\dot{r}_1^2 = \frac{8\pi G \rho_b}{3 r_1} \equiv \frac{\alpha^2}{r_1}, \tag{1}$$

$$\dot{r}_2^2 = \frac{8\pi G \rho}{3 r_2} + \epsilon^2 \equiv \frac{\alpha^2}{r_2} + \epsilon^2, \tag{2}$$

where G is Newton's gravitational constant, α is a constant that includes ρ_b, while ϵ quantifies the excess of ρ above the background field ρ_b. The solution for equation 1 is the same as for the expansion of an Einstein-de Sitter (matter dominated) Universe can be expressed as $r_1(t) \propto t^{2/3}$. Region 1 therefore continues to expand monotonically with time t, suggesting that the linear background solution does not lead to gravitational collapse, as graphically displayed in figure 1. Conversely, the overdensity in region 2 is sufficient for gravity to overcome the cosmological expansion of the Universe, resulting in a turnaround point, followed by the collapse of the mass cloud. Despite including the non-linear perturbative terms in the solution of equation 2, the STHC model predicts that region 2 would collapse to a singularity, as shown by the dashed black line in figure 1 (Binney & Tremaine, 1987; Peacock, 1999).

Realistically, even at early times in the evolution of the Universe, dark matter overdensities are unlikely to display

a perfect isotropy and spherical symmetry. As a consequence, the evolution of region 2 may also be affected by anisotropies that would prevent the cloud to collapse singularly, leading to the formation of subhalos that will interact gravitationally and merge into larger objects. During this phase, known as *virialisation* of the dark matter halo, the mass cloud reaches densities of $\rho \approx 200 \ \rho_b$ and its average radius continues to oscillate about the *virial radius*, labelled R_{200} in figure 1. In absence of external interactions, the substructures in the dark matter halo ultimately reach virial equilibrium. Such halo is hence called *relaxed*, as the most stable orbital configuration of the subhalos does not involve frequent merger events, differently from earlier stages of its evolution (Binney & Tremaine, 1987; Lacey & Cole, 1993; Peacock, 1999).

As indicated in figure 1, the dark matter halo collapses and starts to virialise when $\rho \approx 200 \ \rho_b$ and $r_2 \sim R_{200}$. Assuming spherical symmetry by virtue of the STHC model, the virial mass can be specified from these definitions as

$$M_{200} = \frac{4\pi}{3} R_{200}^2 \times 200 \rho_{cr}, \tag{3}$$

where ρ_{cr} is the critical density of a flat ΛCDM Universe and is chosen to equal ρ_b in $\mathcal{N}$-body simulations.

It has been observed (e.g. Dressler & Shectman 1988; Porter & Raychaudhury 2005; Merluzzi et al. 2015) that large galaxy clusters, similar to those in the MACSIS catalogue, heavily interact with the surrounding filaments and sheets of the cosmic web. As a consequence, the mutual gravitational influence can cause small dark matter halos formed along filaments and sheets to fall into the deeper potential wells of larger halos. This implies that the central halo can accrete mass from their neighbourhood, observed as an infall of substructures that perturbs the system.

An example of such scenario can be observed in the largest galaxy cluster of the MACSIS HYDRO simulation. Figure 2 reports the density map of the hot gas (tracing dark matter halos), rendered through a colour coding. The right-hand side panel in figure 2 shows a schematic of the infall of the smaller surrounding halos towards the central ICM.

2.2 Substructures in the MACSIS simulation

The MACSIS simulation, developed by Barnes et al. (2015, 2017), was run using the Lagrangian TreePM-SPH version of GADGET-3, one of the most widely implemented tools for modelling dark matter halos with Smoothed Particle Hydrodynamics (SPH) of gas clouds (Springel et al., 2001a; Springel, 2005). The data relative to the MACSIS clusters used in this work are the result of a three-stage pipeline.

The first stage involved a low-resolution DMO run, named *parent simulation*, with particles arranged in a 3.2 Gpc box and displaced according to a seed velocity field (see Jenkins 2010, 2013; Jenkins & Booth 2013; Barnes et al. 2017 for details). The evolution of this set of particles was then simulated from redshift $z = 127$ to $z = 0$. The regions of space with the highest density of particles were hence identified and delimited using the Friends-of-Friends algorithm (Davis et al., 1985), which identifies groups of particles based on their mutual separation in space. The
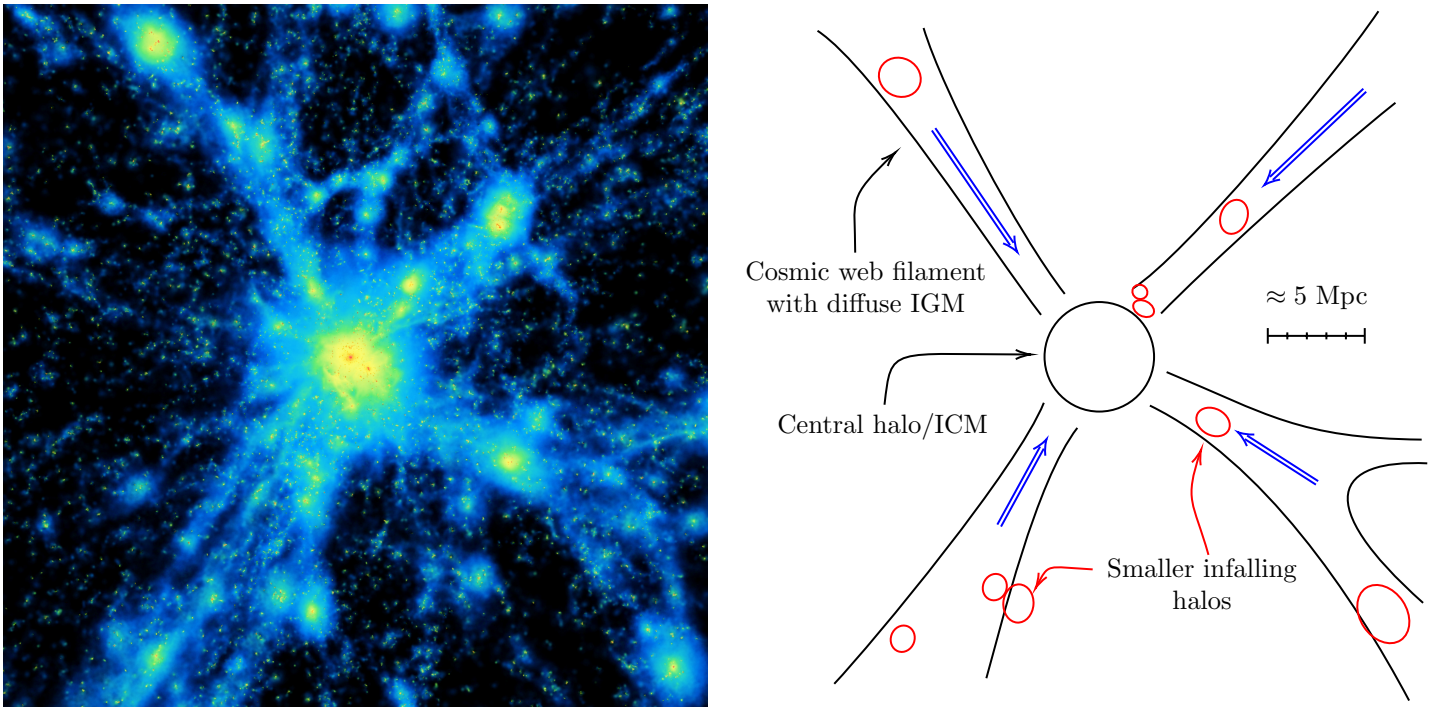
Figure 2: Left: visualisation of the gas distribution in largest MACSIS halo and the surrounding cosmic web filaments at redshift $z = 0.57$, populated with smaller halos. The colour coding expresses the density of the gas, ranging from blue (diffuse) to red (dense). A 3D visualisation of of the galaxy cluster is available at the following link. Right: schematic relative to the figure on the left, highlighting the predominant halos and their infall towards the cluster. The IGM associated with the main halo is known as ICM and is marked by the central black circle, while the IGM associated with smaller objects is marked in red. The figure also displays the diffuse IGM arranged along the filaments of the cosmic web. Image and animation created using the `glnemo` software and PGF/Ti*kz* modules.

dark matter halos having mass exceeding $10^{15}M_\odot$ were then arranged in mass bins and sampled as described in Barnes et al. (2017, section 2 and appendix A). This process selected 390 clusters out of 9754 flagged objects and guaranteed that the abundance bias towards the clusters below a mass $M < 10^{15.6}M_\odot$ was minimised. This step is relevant for results involving the combination of data from different MACSIS halos, as presented in later sections.

Each MACSIS halo in the catalogue was then simulated again with DMO and HYDRO settings, enhancing the resolution of a smaller spherical volume ($5 \times R_{200}$ in radius) centred on the cluster. This technique, known as *zoom simulation*, characterises the second stage, which also deploys the astrophysical processes occurring at scales below the MACSIS mass resolution limit, $7.40 \times 10^9 M_\odot$, and the length resolution limit, ≈ 4 kpc (see also McCarthy et al. 2017). These effects, including stochastic star formation, stellar winds and shock-heated gas from Active Galactic Nuclei (AGN feedback) and supernovae, are classified as *sub-grid physics* and have been relevant for the interpretation of stellar and baryon fractions of MACSIS objects (Henson et al., 2017; Altamura, 2019; Murin, 2019). The AGN feedback implemented in MACSIS follows the methodology introduced by Booth & Schaye (2009), which consists in identifying the $n_{heat} = 20$ gas particles closest to the AGN seed and increasing their temperature by $\Delta T_{heat} = 10^{7.8}$ K (Barnes et al., 2017).

After the second stage, the processing of the MACSIS DMO and HYDRO datasets was complete. However, the identification of subhalos within the MACSIS galaxy clus-

ters required a third (post-processing) stage, operated using the `SUBFIND` code (Springel et al., 2001b). Given a distribution of particles, `SUBFIND` was able to estimate the local mass density and define isodensity surfaces in three dimensions. The surfaces, delimited by a saddle point in the density field, mark the boundaries of a *subhalo*. By considering Poisson's equation for the gravitational potential and a density field, this description implies that all the particles selected by `SUBFIND` are gravitationally bound to their respective subhalos (see also Altamura 2019; Murin 2019). As a result, each MACSIS halo will present a `SUBFIND` catalogue, describing the kinematics, thermodynamics and composition of the particles bound to the substructures, which might be located within the central cluster, but might also constitute the population of smaller objects with their associated IGM. From this point onwards, all halos (strictly within or outside the main cluster) identified by `SUBFIND` will be referred to as *subhalos* or *subgroups*.

As anticipated by Springel et al. (2001b), the reliable identification of subhalos is a challenging procedure. In particular, the `SUBFIND` code only accounts for the static distribution of particles and ignores their velocity information. This limitation may affect the results for subhalos with low particle count ($\mathcal{N} \lesssim 20$), while still offer an accurate picture for substructures having higher particle count.

2.3 Astrophysics of the Sunyaev-Zel'dovich effects

With temperatures reaching $T \sim 10^7 - 10^8$ K, a large fraction of the hot IGM is expected to be composed by ionised
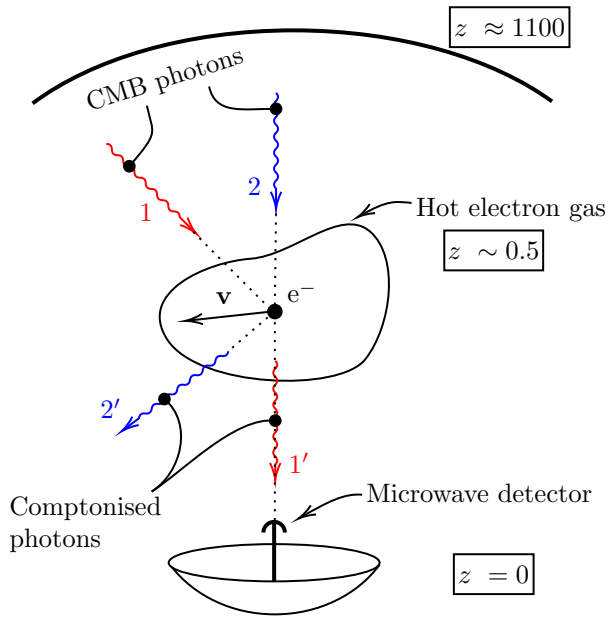
Figure 3: Schematic of the inverse Compton scattering of two CMB photons, labelled 1 and 2, off electrons in a hot ionised gas. The velocity **v** of the electrons is assumed to follow a non-relativistic Maxwell-Boltzmann distribution. Although being previously aligned with the observer's line of sight, as a consequence of the scattering photon 2 is deflected into 2', while being replaced by photon 1', which had entered the IGM from a different angle. The process illustrated in this figure does not involve the simultaneous interaction of two photons with an electron. Double comptonisation is not contemplated in this work, but further details can be found in Jauch & Rohrlich (1976); Rybicki & Lightman (1979); Fisenko & Lemberg (2018). Image created using PGF/Ti*kz* modules and adapted from Sunyaev & Zeldovich (1972).

hydrogen and helium gas, which gives rise to free/free X-ray emission (e.g. Powell et al. 2009; Allen et al. 2011), but also a microwave signature, known as SZ effect. This phenomenon arises from the interaction between the low-energy photons of the CMB and the high-energy electrons in the ionised IGM through *inverse Compton scattering* (Lightman & Rybicki, 1979a,b, 1980; Sarazin, 1986). Figure 3 contains a schematic of the scattering process, in which two CMB photons, labelled 1 and 2, interact with electrons in the IGM of a galaxy cluster. During the process, the energy imparted on the photons by electrons can be expressed in terms of an increase in frequency from ν to ν', according to

$$\frac{\nu'}{\nu} = \frac{1 - \beta\mu}{1 - \beta\mu' + \frac{h\nu}{\gamma m_e c^2}(1 - \mu_{\rm sc})} \approx \frac{1 - \beta\mu}{1 - \beta\mu'}, \qquad (4)$$

where $\beta = v/c$ indicates the ratio between the speed v of the photons and the speed of light in vacuum c, h is the Planck constant, m_e the mass of the electron, $\gamma \equiv (1 - \beta^2)^{-1/2}$ is the Lorentz factor, μ is the cosine of the angle of the incoming CMB photon, μ' the cosine of the angle of the comptonised photon and lastly $\mu_{\rm sc}$ is the cosine of the angle between the incoming and outgoing photon (Illarionov & Syunyaev, 1972; Jauch & Rohrlich, 1976; Rybicki & Lightman, 1979; Lightman & Rybicki, 1979b,a, 1980; Sarazin, 1986). The right-hand side of equation 4 reports the non-relativistic approximation, which is used
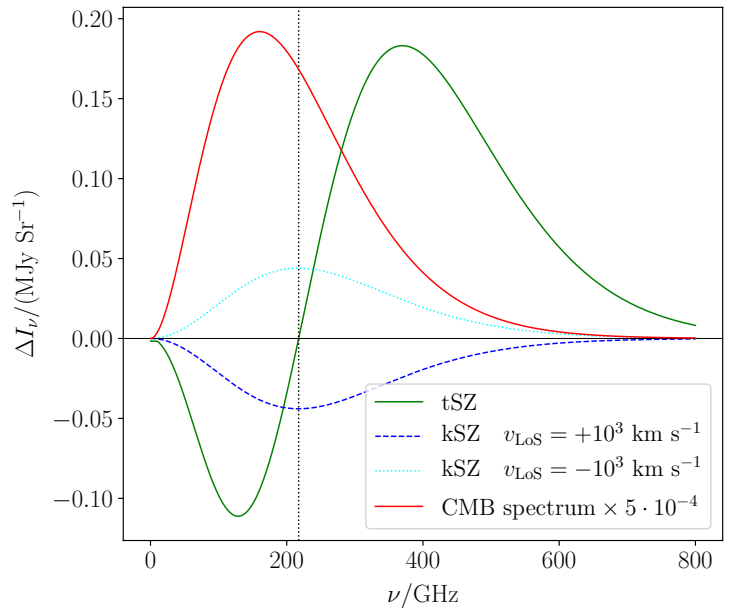

Figure 4: Plot displaying the comparison of the spectral distortions for the tSZ (green solid curve) and kSZ (blue dashed and dotted lines) against the spectrum of the CMB downscaled by a factor 5×10^{-4} (red solid curve). The tSZ spectrum was computed using $y_{\rm tSZ} = 10^{-4}$. The kSZ instead was simulated with $y_{\rm kSZ} = 10^{-5}$ for an object moving with velocity along the line of sight (LoS) $v_{\rm LoS} = \pm 10^3 {\rm km \ s^{-1}}$ (positive is defined as towards the observer). The vertical dotted line marks the turnover of the tSZ at $\nu \approx 217$ GHz, where the tSZ deviation from the CMB spectrum is expected to vanish. Image created using `matplotlib` and adapted from Birkinshaw (1999); Carlstrom et al. (2002); Mroczkowski et al. (2019).

in the derivation of the SZ spectral distortion in the case of non-relativistic plasmas.

By applying the equation for inverse Compton scattering to a cloud of hot electrons governed by a non-relativistic Maxwell-Boltzmann distribution and using a generalised form of the Kompaneets equations (1956), Sunyaev & Zeldovich (1970c) derived for the first time the distortion ΔI_v in the spectrum of the CMB caused by the energy transfer of its photons during comptonisation. This spectral signature, known as thermal SZ (tSZ) effect, is predicted to cause a decrement in photons below $\nu \approx 217$ GHz, complemented by an increment in photon count above this threshold. The shape of tSZ distortion is displayed by the green solid line in figure 4 and corresponds to the equation

$$\Delta I_v \approx I_0 y \frac{x^4 e^x}{(e^x - 1)^2} \left(x \frac{e^x + 1}{e^x - 1} - 4 \right) \equiv I_0 y g(x), \qquad (5)$$

where one can define

$$I_0 = 2\frac{(k_B T_{\rm CMB})^3}{(hc)^2} = 270.33 \left[\frac{T_{\rm CMB}}{2.7255 \ {\rm K}} \right]^3 \ {\rm MJy \ sr^{-1}} \quad (6)$$

and

$$x \equiv \frac{h\nu}{k_B T_{\rm CMB}}, \qquad (7)$$

with $T_{\rm CMB}$ the CMB temperature, k_B the Boltzmann con-

stant and y_{tSZ} the tSZ Compton parameter

$$y_{\mathrm{tSZ}} \equiv \int_{\mathrm{LoS}} \frac{k_{\mathrm{B}} T_{\mathrm{e}}}{m_{\mathrm{e}} c^2} \mathrm{d}\tau_{\mathrm{e}} \tag{8}$$

$$= \int_{\mathrm{LoS}} \frac{k_{\mathrm{B}} T_{\mathrm{e}}}{m_{\mathrm{e}} c^2} n_{\mathrm{e}} \sigma_{\mathrm{T}} \mathrm{d}l \tag{9}$$

$$= \frac{\sigma_{\mathrm{T}}}{m_{\mathrm{e}} c^2} \int_{\mathrm{LoS}} P_{\mathrm{e}} \mathrm{d}l \ . \tag{10}$$

The equations above show that y_{tSZ} can be recast in terms of the optical depth τ_{e} of the IGM or by integrating the (classical) electron gas pressure P_{e} of the line elements $\mathrm{d}l$ along the direction of observation, or alternatively by considering the electron temperature T_{e}, the electron number density n_{e} and the Stefan–Boltzmann constant σ_{T} (Zeldovich & Sunyaev, 1969; Sunyaev & Zeldovich, 1969, 1970a,b,c, 1972; Birkinshaw, 1999; Carlstrom et al., 2002; Mroczkowski et al., 2019).

In the case of the tSZ effect, y_{tSZ} is obtained by integrating the mass-weighted temperature of infinitesimal volumes of the IGM. A detailed derivation of the y_{tSZ} in discrete domain can be found in section 4.1.

As shown by equation 4 and suggested by figure 3, the derivation of the tSZ Compton parameter clearly depends on the velocity distribution of the ensemble of electrons. For a gas in local thermal equilibrium, the Maxwell-Boltzmann distribution implies that the average velocity of the particles must vanish, i.e. $\langle \boldsymbol{\beta} \rangle = \mathbf{0}$. This implies that the tSZ effect must arise from the second moment of the distribution $\langle \|\boldsymbol{\beta}\|^2 \rangle > 0$. However, the galaxy cluster may exhibit a *bulk motion* in the rest frame of the CMB, which introduces an additional constant term $\boldsymbol{\beta}_{\mathrm{p}}$ in the calculation of the velocity distribution (e.g. Sunyaev & Zeldovich 1980). This scenario translates into an additional monopole component of the SZ effect, known as *kinetic* SZ (kSZ) distortion. Similarly for y_{tSZ}, the derivation for the kSZ effect leads to a spectral distortion given by

$$\Delta I_v \approx -I_0 \frac{x^4 \mathrm{e}^x}{(\mathrm{e}^x - 1)^2} y_{\mathrm{ksZ}} \tag{11}$$

and a y_{kSZ} parameter

$$y_{\mathrm{ksz}} \equiv \int_{\mathrm{LoS}} \sigma_{\mathrm{T}} n_{\mathrm{e}} \boldsymbol{n} \cdot \boldsymbol{\beta}_{\mathrm{p}} \mathrm{d}l = \int_{\mathrm{LoS}} \boldsymbol{n} \cdot \boldsymbol{\beta}_{\mathrm{p}} \mathrm{d}\tau_{\mathrm{e}}, \tag{12}$$

which is sensitive to the component of $\boldsymbol{\beta}_{\mathrm{p}}$ along the observer's line of sight (LoS), i.e. $\boldsymbol{n} \cdot \boldsymbol{\beta}_{\mathrm{p}}$ (Sunyaev & Zeldovich, 1980, 1972; Birkinshaw, 1999; Carlstrom et al., 2002; Ruan et al., 2013; Adam et al., 2017; Mroczkowski et al., 2019).

Unlike the tSZ effect, the kSZ signature is direction-dependent and can lead either to a deficit or a boost in CMB photons, according to the sign of peculiar velocity of the gas along the LoS (see figure 4). From an observational standpoint, both the tSZ and kSZ distortions can be measured as fluctuations ΔT_{CMB} in the temperature of the CMB caused by the foreground galaxy cluster, which can be expressed as

$$\frac{\Delta T_{\mathrm{CMB}}}{T_{\mathrm{CMB}}} \approx y_{\mathrm{tSZ}} \left(x \frac{\mathrm{e}^x + 1}{\mathrm{e}^x - 1} - 4 \right) = y_{\mathrm{tSZ}} \ f(x) \tag{13}$$

for the tSZ distortion and

$$\frac{\Delta T_{\mathrm{CMB}}}{T_{\mathrm{CMB}}} \approx -y_{\mathrm{kSZ}} \tag{14}$$

for the kSZ signal.

Isolating kSZ signatures has been proved to be a complex task for two main reasons. Typical peculiar velocities of galaxy clusters are expected to be $\sim 10^2$ km s^{-1}, leading to $y_{\mathrm{kSZ}} \sim 10^{-5}$, which predicts a ~ 27 μK deviation from the CMB temperature. Detecting μK-scale fluctuations with reliable signal-to-noise ratio constitutes the first challenge. The second difficulty lies in the functional form of the kSZ spectrum, which is mathematically equivalent to that of a blackbody. This characteristic causes unavoidable confusion between foreground kSZ fluctuations and physical anisotropies of the CMB. Over the last two decades, several techniques have been developed to disentangle the microwave components of the tSZ and kSZ effects from the CMB and contaminations from other foregrounds (Chluba & Sunyaev, 2004; Stebbins, 2007; Chluba et al., 2012; Sunyaev & Khatri, 2013; Adam et al., 2017). This advancement, in synergy with the recent advent of KID detectors, allowed the reliable reconstructing the peculiar velocities of galaxy clusters (e.g. Ruan et al. 2013) and, most importantly, the peculiar velocities of subhalos within large galaxy cluster mergers (e.g. Adam et al. 2017), which are the main focus of this work. In analogy with the MACS J0717.5+3745 cluster ($z \approx 0.55$), object of recent studies by Limousin et al. (2012, 2016); Adam et al. (2017); Jauzac et al. (2018), the redshift of the MACSIS halos drawn from the simulation was chosen to be $z = 0.57$.

3 Thermodynamics of the hot gas and ionisation fraction

Although the dark matter dominates the evolution of galaxy clusters on large scales, its distribution can only be reconstructed using indirect observations, e.g. weak gravitational lensing (Powell et al., 2009; Henson et al., 2017; Jauzac et al., 2018). However, the ionised hot IGM is known to interact with the microwave CMB photons, in addition to being a source of X-rays. The observation of galaxy clusters in microwave bands is therefore one of the two crucial probes for the thermodynamics of the hot gas (Birkinshaw, 1999; Carlstrom et al., 2002; Mroczkowski et al., 2019).

As discussed in section 2.1, as an overdense dark matter halo collapses under gravity, the gas traces it and will collapse in the same way. During this process, the velocity of the gas particles increases by virtue of the virial theorem. The the collisional nature of the IGM implies that the temperature of the gas will also increase, until the pressure from the gas balances the gravitational attraction. This scenario describes a collapsed cloud in hydrostatic equilibrium, which coincides with its dark matter halo being virialised (see figure 1). Assuming the ideal gas law, the hot gas of such galaxy cluster will therefore show a mean temperature, also called *virial temperature* T_{200}, given by

$$T_{200} = \frac{2}{3} \left(\frac{4\pi}{3} \right)^{1/3} \mu m_{\mathrm{P}} \ GM_{200}^{2/3} \ \rho_{cr}^{1/3}, \tag{15}$$

where μm_{P} is the mean molecular weight of the gas and m_{P} is the mass of the proton. Although T_{200} gives an estimate

of the average temperature of the IGM, hydrodynamical simulations implement a distribution of temperatures (i.e. non-isothermal), revealing a large scatter of the particle temperatures about this characteristic value (Davé et al., 2001; Valageas et al., 2002). The temperature distribution is also correlated with a large scatter in the local gas density. The average behaviour of the IGM temperature T as a function of density can be computed for an ideal gas (see e.g. Valageas et al. 2002), leading to the equation of state of the hot IGM, which can be expressed as

$$T(\rho) \simeq T_{200} \left[\left(\frac{\rho}{\rho_{cr}} \right)^{1/3} - 1 \right]. \qquad (16)$$

Figure 5 shows the equation of state of the hot IGM plotted in the (T, ρ) diagram, also known as phase diagram. As suggested by equation 15, the height of the turn-over for the equation of state of the hot IGM is controlled by $T_{200} \propto M_{200}^{2/3}$, which implies that more massive virialised IGM gas will appear in the top-region of the phase diagram, aligned with the $\rho \approx 200\rho_{cr}$ line, as noted in section 2.1. Two galaxy clusters with different masses will therefore contain gravitationally heated gas populating regions of the (T, ρ) diagram as shown in figure 5. If thermal interaction occurs between such objects, the regions occupied by the hot IGM will overlap and blend into a single one.

An important process that influences the morphology (T, ρ) diagram is the AGN feedback, implemented in MACSIS as part of the sub-grid physics. As presented in Booth & Schaye (2009) and remarked by Barnes et al. (2017), the AGN feedback purely acts on the temperature of the particles in the surroundings of the AGN seed. This implies that the simulated process is purely thermal, with no AGN outflow modelled as an increase in the particles' kinetic energy. The gas particles heated through this process will therefore be displaced away from the centroid of the gravitationally heated region (see figure 5), towards the top left corner of the diagram. Once inside this region, the gas particles will enter a regime where the typical cooling time becomes $\sim 10 - 100$ Gyrs (see figure 5 in Dalla Vecchia & Schaye 2012). As a consequence, the majority of them will not leave this thermodynamic state within one Hubble time, while still being exposed to further AGN heating events, with the possibility of attaining up to $T \sim 10^{8.7}$ K.

Figure 5 shows the position additional features that can be observed in the (T, ρ) diagram of the gas in a galaxy cluster, which do not constitute a central part of the present work and will not be analysed in detail. The gas in radiative equilibrium with the UV background mostly characterises the (T, ρ) distribution below $T \simeq 10^5$ K and with $\rho \gtrsim 200\rho_{cr}$ (e.g. Valageas et al. 2002), alongside with the equation of state of the cooled condensed gas, which is associated with the formation of galaxies and stars. In the case of MACSIS, the equation of state of the condensed gas is imposed in the simulation and is part of the modelling of the sub-grid physics (Schaye et al., 2010; Dalla Vecchia & Schaye, 2012; McCarthy et al., 2017; Barnes et al., 2017).

In the context of hydrodynamical simulations of galaxy clusters, the study of the thermodynamic phase diagrams is a useful diagnostics to assess the reliability of the astrophysical processes implemented in the modelling. However,
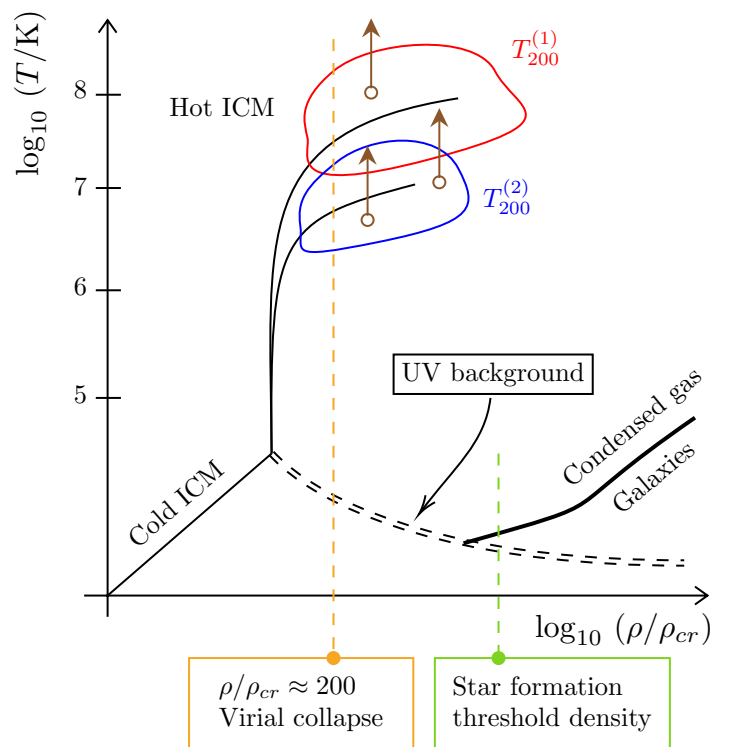

Figure 5: Example of the IGM phase diagram for two galaxy clusters, labelled 1 and 2, for which $T_{200}^{(1)} > T_{200}^{(2)}$. The black straight line on the lower-left corner of the graph shows the equation of state of the cold IGM (see Valageas et al. 2002 for further details). The equation of state for the hot IGM is marked for two different values of T_{200} by the curved black lines. The regions marked by the red and blue contours indicate the position of the majority of the hot gas particles in the IGM, in correspondance of $T \sim 10^7 - 10^8$ K and $\rho \gtrsim 200\rho_{cr}$ (orange dashed line). The diagram shows also the line of the ionisation equilibrium due to the UV background (double-dashed black lines), the threshold density for star formation (Schaye et al., 2010; Dalla Vecchia & Schaye, 2012; McCarthy et al., 2017) and the equation of state of the cooled condensed gas, correlated to the formation of galaxies (Dalla Vecchia & Schaye, 2012; McCarthy et al., 2017). Ultimately, the brown upward arrows indicate the increase in temperature of gas particles involved in AGN heating processes. The length of the arrows is representative to the $\Delta T_{heat} = 10^{7.8}$ K used in MACSIS (Barnes et al., 2017). Image created using PGF/Ti*k*z modules.

following from section 2.3, the (T, ρ) diagram suggests which gas particles have a sufficient temperature to dominate the contribution to the tSZ. Figure 6 displays the combined (T, ρ) diagram for particles in the 390 MACSIS clusters. Only the particles orbiting within a $5 \times R_{200}$ spherical region centred on the main cluster were selected, in order to restrict the analysis to the high resolution region, as discussed in section 2.2. Once having converted the density data from comoving into physical units, the data points were sampled to form a 2D histogram and plotted for all particles simulated with high resolution, i.e. ICM and subhalo IGM. After removing the contribution of the ICM at temperature $T_{200} \simeq 10^8$ K, the subhalo component emerges in the upper region of the plot on the right (figure 6). The main feature at $T \simeq 10^7$ K can immediately be associated with the gravitational heating of the gas bound to subhalos. However, the upper region towards $T \simeq 10^8$ K
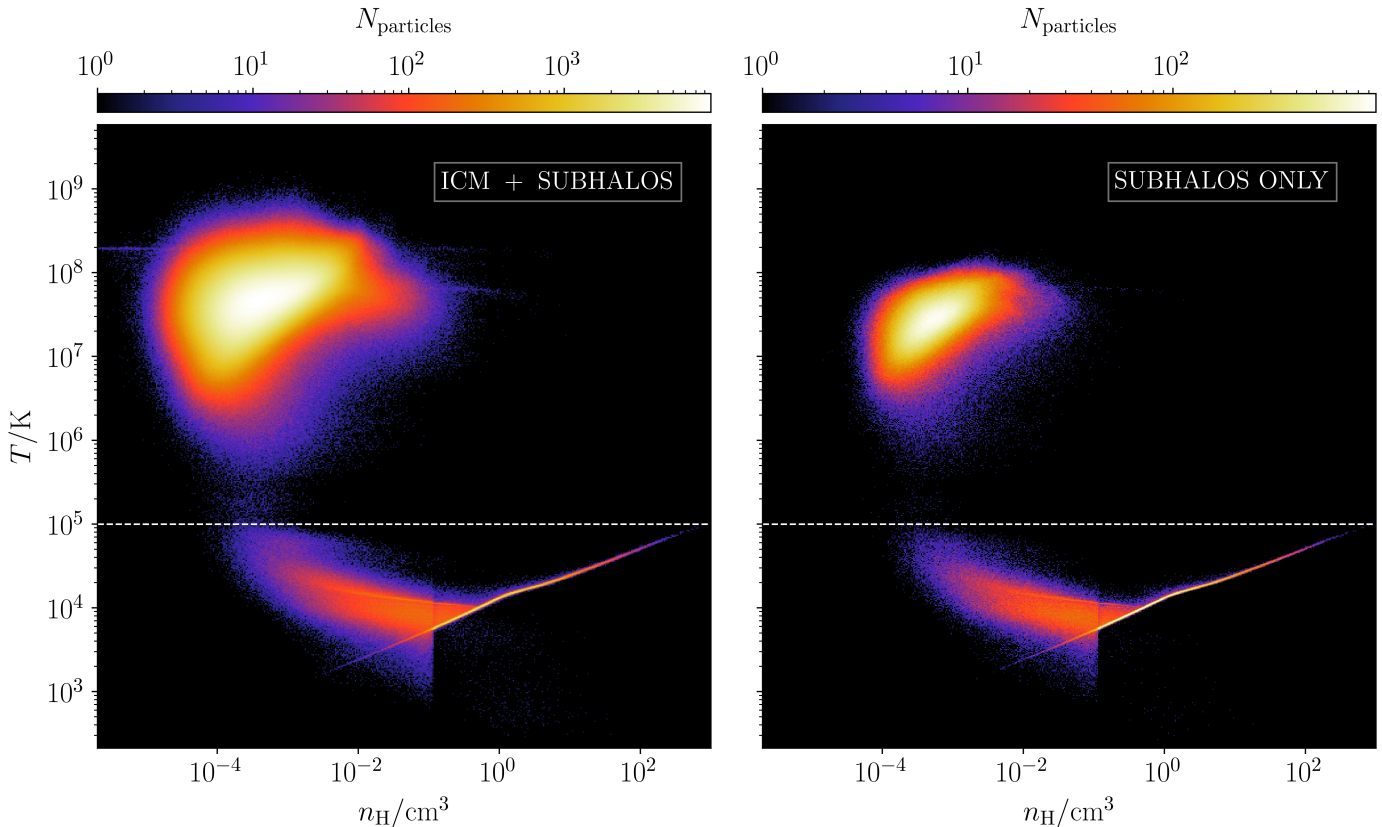
Figure 6: Phase diagrams, scaled in terms of the hydrogen nuclei number density n_{H}, showing all high resolution gas particles in the 390 MACSIS halos (left) and selecting only IGM gas particles bound to subhalos (right). Each bin in the map is colour coded according to the number of gas particles within the bin, divided by its area in appropriate units. The dashed white line delimits the cold gas $T < 10^5$ K from the hot gas $T > 10^5$ K. In the subhalo-only diagram, the group of particles at the $T \simeq 10^7$ K level corresponds to the gravitationally heated gas, while the ICM of the main cluster (left) appears one order of magnitude hotter. In the cold diffuse gas regions it is also possible to distinguish the ionisation equilibrium from the UV background, the star formation threshold at $n_{\mathrm{H}} = 0.1$ cm^{-3} (Dalla Vecchia & Schaye, 2012) and the imposed equation of state of condensed gas.

originates from single and multiple heating of gas particles in the neighbourhood of AGN seeds.

Gas particles cooling from the lower portion of the gravitationally heated region or from the UV background band evolve in a fast cooling regime, with time scale of $0.1 - 10$ Myrs (Dalla Vecchia & Schaye, 2012). This implies that at any given redshift snapshot very few particles are likely to be observed in the process of cooling. Instead, the final state of such cooling process will be densely populated and consists in the equation of state enforced for the condensation of gas, as shown by the colour coding of the bottom right region of the plots in figure 6.

As remarked in section 2.3, the comptonisation of CMB photons is favoured in presence of hot plasma, as more energetic electrons will impart a larger energy transfer to the incoming photons. As a consequence, the contribution from low-temperature gas particles to the SZ effect is expected to be highly suppressed. Furthermore, only the fraction of gas that is also ionised effectively participates in the Compton scattering. In order to compute the ionisation fraction, the gas mass was assumed to be entirely composed by hydrogen (H) and helium (He), which is fully ionised for $T > 10^5$ K and non-ionised below this threshold. Despite neglecting the metallicity of the IGM and its contribution to the ionisation fraction, the assumption for the gas chemical composition has been found to be robust in the context of

Compton scattering (see e.g. Rybicki & Lightman 1979; da Silva et al. 2000, 2001a,b; Renzini 2004). The transition between bound and ionised states of the IGM H/He is chosen to follow a step function in temperature, expressed by

$$f(T) = \left\{ \begin{array}{ll} 0 & T < 10^5 \text{ K} \\ 1 & T > 10^5 \text{ K} \end{array} \right., \qquad (17)$$

where $f(T)$ is the ionisation fraction. This selection filters out all the gas particles in the lower region of the phase diagram (found to be $\approx 2\%$ on average), while directing the data for the remaining ones ($\approx 98\%$) to the `Python` modules dedicated to the modelling of the SZ maps, presented in the successive step of the processing pipeline (for details on the software architecture, see appendix A).

Similarly to the IGM metallicity, the assumption of the step function selection has been proven not to introduce significant biases when compared to the full implementation of the Saha equation and independent hydrodynamical tests (Prigogine et al., 1989; Rogers et al., 1996; da Silva et al., 2000, 2001a,b; Renzini, 2004). Under these conditions, it is possible to link the number density of H/He atoms n_{H} to that of electrons n_e:

$$n_e = \kappa_e n_{\mathrm{H}} \equiv \kappa_e \frac{\rho_{\mathrm{H}}}{m_{\mathrm{P}}}, \qquad (18)$$

where m_P is the proton mass, ρ_H the SPH gas density and $\kappa_e \approx 0.88$ is the mean number of ionised electrons per baryon (da Silva et al., 2000).

4 Mapping of SZ signals

Section 3 reported the first stage of the processing pipeline for the construction of SZ maps. The following procedure consists in the computation of the y_{SZ} along an arbitrary line of sight for the MACSIS HYDRO clusters. The results for the tSZ and kSZ will be then compared to the spatial distribution of the gas mass and then processed using a peak-finding algorithm for the identification of the most prominent substructures.

4.1 Discretisation of y_{SZ} integrals

Starting from equation 12, the explicit form of the scalar product $\boldsymbol{n} \cdot \boldsymbol{\beta}_p$ can be written in terms of the proper bulk velocity $\boldsymbol{v}_p$ of the plasma cloud in the CMB rest frame:

$$\boldsymbol{n} \cdot \boldsymbol{\beta}_p \equiv \frac{\boldsymbol{n} \cdot \boldsymbol{v}_p}{c} = \frac{v_{LoS}}{c}. \qquad (19)$$

Let us consider an observer $\mathcal{O}$ steering a microwave instrument towards a galaxy cluster. The angular sampling of the detector results in the subdivision of the region of the sky in pixel-like areas, as displayed in figue 7. Prescription introduced by equation 12 therefore includes the sum of the contribution to y_{kSZ} generated by infinitesimal volumes $dV = A_{pix}dl$ along the LoS. By combining equations 12, 17, 18 and 19, one can obtain

$$y_{kSZ} \equiv \int_{LoS} \sigma_T \, n_e \, \boldsymbol{n} \cdot \boldsymbol{\beta}_p \, dl \qquad (20)$$

$$= \frac{\sigma_T}{c} \int_{LoS} n_e \, v_{LoS} \, dl \qquad (21)$$

$$= \frac{\sigma_T}{m_P c} \, \kappa_e f(T) \times \int_{LoS} \rho_H \, v_{LoS} \, dl \qquad (22)$$

$$= \frac{\sigma_T}{A_{pix} \, m_P c} \, \kappa_e f(T) \times \int_{LoS} v_{LoS} \, \rho_H dV \qquad (23)$$

$$= \frac{\sigma_T}{A_{pix} \, m_P c} \, \kappa_e f(T) \times \int_{LoS} v_{LoS} \, dM_{gas} \qquad (24)$$

$$= \frac{\sigma_T}{A_{pix} \, m_P c} \, \kappa_e f(T) \times \lim_{N_{LoS} \to \infty} \sum_{i=0}^{N_{LoS}} v_i M_i \qquad (25)$$

$$\stackrel{!}{=} \frac{\sigma_T}{A_{pix} \, m_P c} \, \kappa_e f(T) \times \sum_{i=0}^{N_{gas}} v_i M_i \,, \qquad (26)$$

where the integral has been replaced by a summation of N_{LoS} volume elements along the LoS and successively by the sum of the LoS momenta of the N_{gas} gas particles within the projected volume.
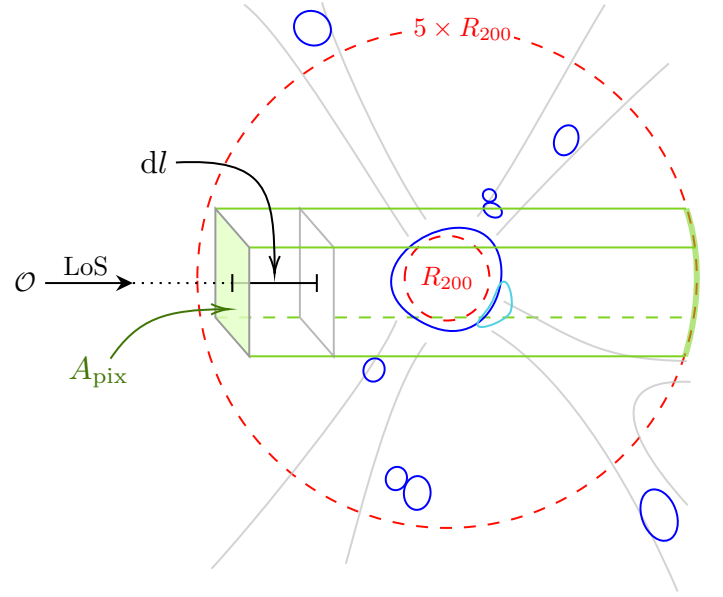

Figure 7: Geometry of the projection of a galaxy cluster on the plane of the sky, as observed by $\mathcal{O}$. A volume, defined by the solid and dashed green lines, intercepts the ionised gas distribution along the LoS. The cross sectional area of the volume is A_{pix} and its length is subdivided into infinitesimal depths dl. As seen by $\mathcal{O}$, the volume spans from the front boundary of the $5 \times R_{200}$ high resolution region to the far side boundary. Similarly to figure 2, the blue solid lines represent the ICM and subhalo IGM, while the solid grey lines mark the schematic contours of the surrounding filaments of the cosmic web. Moreover, in cyan color is displayed a particular example of a subhalo in the process of entering the ICM. Image created using PGF/Tikz modules.

Similarly, the computation of the tSZ Compton y-parameter in discrete domain can be written as

$$y_{tSZ} \stackrel{!}{=} \frac{\sigma_T k_B}{A_{pix} \, m_P m_e c^2} \, \kappa_e f(T) \times \sum_{i=0}^{N_{gas}} T_i M_i \,, \qquad (27)$$

which expresses the mass-weighted temperature of the gas particles, summed over the projected volume illustrated in figure 7 (e.g. da Silva et al. 2000).

4.2 SZ maps of MACSIS galaxy clusters

Equations 26 and 27 allow the calculation of SZ maps, relative to an arbitrary projection perpendicular to the observer's LoS. However, it is necessary to evaluate A_{pix} and decompose of v_{LoS}, in order to produce reliable SZ maps.

As drawn in figure 7, the area A_{pix} can be expressed in physical units as Mpc^2. However, it is often useful to convert the physical scale in the projection to angular scale, by using the redshift-dependent *angular diameter distance* $d_A(z)$ (see e.g. Peacock 1999 for full details). It is then possible to write A_{pix} [arcmin^2] = $(180 \times 60/\pi)^2 \, A_{pix}$ [Mpc^2]$/d_A^2(z)$ and analogously for converting any linear distance on the plane of the sky into units of arcminutes.

The velocity of subhalos in the rest frame of te CMB can be composed by two terms: the bulk motion of the host galaxy cluster and the peculiar velocity of the subhalo relative to the ICM. The post-processing pipeline developed

for this project includes a `Python` module, named `cluster profiler`, with methods for averaging the velocity of all the particles (including non-gas types, see e.g. Altamura 2019; Murin 2019) within the high resolution region and returning the bulk motion of the parent cluster in the CMB rest frame. The difference between the subhalo velocities stored by `SUBFIND` and the cluster proper motion delivers the velocity of subhalos in the cluster's rest frame. Since the peculiar velocity of galaxy clusters are expected to be ~ 100 km s^{-1}, the contribution to $y_{\rm kSZ}$ is expected to be comparable to that of subhalos in the cluster's frame and hence non negligible (Mroczkowski et al., 2019). Indeed, the parent halo's bulk motion can introduce a bias in the distribution of velocities, since it can boost the kSZ signal if the subhalo is moving in the same direction of the central cluster, while the y-parameter would be suppressed in the opposite case.

After building the datasets with the parameters required for the computation of $y_{\rm tSZ}$ and $y_{\rm kSZ}$, the mock maps were subdivided into projected angular square pixels and ultimately convolved via a Point Spread Function (PSF) kernel that simulates the forward beam of a microwave telescope. As introduced in section 1, the instrument of interest in this work was IRAM's NIKA camera, which has been recently upgraded to the NIKA-2 configuration (Catalano et al., 2018). As a result of the commissioning of this facility, Catalano et al. (2018) reported a PSF with a full width at half maximum of 17.7 ± 0.1 arcsec, measured with the 150 GHz KIDs array.

In order to reliably reproduce the NIKA-2 PSF convolution, the maps of the MACSIS galaxy clusters were sampled with $N_{\rm bins}^2 = 600^2$ square bins. The angular size of each bin was measured to be 6.4 arcsec, which allowed to oversample the PSF area with four bins, in compliance with the Nyquist sampling theorem. The oversampling of the SZ maps was implemented using the `numpy.histogram2d` method, while a Gaussian convolution kernel was introduced using the `astropy.convolution.Gaussian2DKernel` functionality, both called from a higher-level module developed for the generation of SZ maps from MACSIS data (see appendix A).

Figure 8 shows the result of the pipeline for the generation of mock SZ maps of the MACSIS halo 0, rendered at the NIKA-2 (150 GHz) resolution. The maps include both the contribution from the central ICM and the hot IGM bound to the subhalos. As stated in sections 1 and 2.3, the values of $y_{\rm tSZ} \sim 10^{-4}$ are expected to emerge close to the centre of the ICM, where the deep gravitational potential favours the highest concentration of mass and therefore the highest temperature. As predicted in Altamura (2019) and Murin (2019), the abundance of subhalos outside the R_{200} sphere is evident in the maps reported in figure 8, with numerous peaks tracing IGM overdensities associated with $y_{\rm tSZ} \sim 10^{-5} - 10^{-6}$. The kSZ maps instead display the fluctuations of the kSZ Compton parameter, associated with subhalos moving away (red colour scheme) and towards the observer (blue colour scheme). A left-handed Cartesian coordinate system was adopted in the SZ maps, so that the positive direction of the axis perpendicular to the plane of the sky is defined to be away from the ob-

server. The computation of the velocity field for the kSZ map in figure 8 was performed by removing the monopole component given by the bulk motion of the whole cluster in the CMB rest frame. The velocity field of the subhalos, visualised in terms of $y_{\rm kSZ}$, is therefore calculated in the rest frame of the cluster and represents the proper motion of the substructures. By comparing the kSZ map with the relative colour coding, it is possible to observe that the largest fluctuations can reach $y_{\rm kSZ} \sim 10^{-5} - 10^{-6}$, which makes their detection more reliable than those with smaller mass or LoS velocity.

4.3 Detection of SZ fluctuations

The maps of kSZ and tSZ signals based on the MACSIS simulation data can be regarded as the result of ideal observations, conducted with a microwave telescope having the same PSF as NIKA-2 and free from any systematic bias or source of noise. After having successfully decoupled the tSZ and kSZ components from other astrophysical signals, a hypothetical observer would attempt to detect fluctuations in the maps, with the aim of reconstructing the temperature and velocity fields associated with the target galaxy cluster.

In line with the observer's approach, a peak detection algorithm was implemented on the kSZ maps, in order to identify, flag and retrieve information about the signal fluctuations in an automated fashion. As in the observer's case, the fluctuation detection method was solely based on $y_{\rm kSZ}$ as a function of two angular coordinates. The algorithm introduced in this work is commonly known as Laplacian of Gaussians (LoG) and involves a convolution kernel which enhances fluctuations of given scales above a background (see e.g. Chen et al. 1987; Kong et al. 2013). The LoG approach was implemented using the functionalities from `skimage`, a `Python` package dedicated to feature recognition and image processing.

The construction of the algorithm follows the prescription given in Kong et al. (2013). Assuming a target feature of size σ, the image is firstly convolved with a 2D Gaussian kernel, which has the effect of smoothing the fluctuations of sizes $\lesssim \sigma$. The convolved image is then arithmetically subtracted from the original one, in order to suppress the large-scale background features and retaining the fluctuations of size $\lesssim \sigma$. Up to this stage, the procedure is identical to the *unsharp masking algorithm*, which is used to identify the position of fluctuations centroids (see e.g. Gonzalez et al. 2009; Powell et al. 2009 for details). However, the LoG involves a second stage, which aims at enhancing and detecting the edges of fluctuations using the Laplacian operator as a spatial filter.

The two-stage convolution can be mathematically regarded as one operation, performed with an overall kernel given by

$$\nabla^2 G(x,y) = -\frac{x^2 + y^2 - 2\sigma^2}{\pi \sigma^4} \exp\left(-\frac{x^2 + y^2}{2\sigma^2} \right), \quad (28)$$

where $G(x,y)$ is a 2D Gaussian represented in the image coordinates (x,y) (Chen et al., 1987; Kong et al., 2013). This convolution kernel is appropriately constructed to detect bright features on backgrounds and assumes that the peaks have a circular symmetry in the plane of the image.
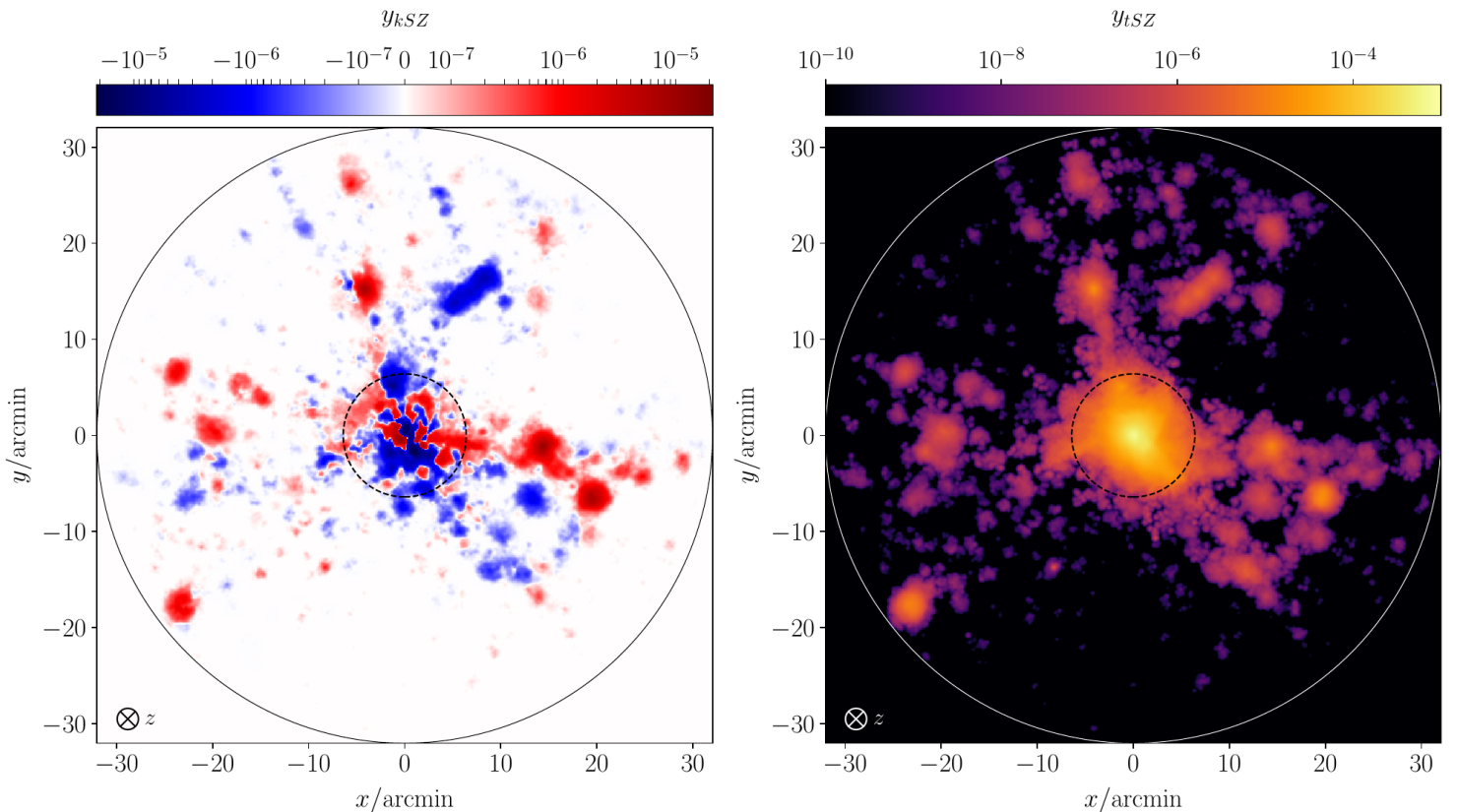
Figure 8: SZ maps relative to the MACSIS halo 0 at redshift $z = 0.57$, displayed with a field of view of $5 \times R_{200}$. The left image shows the kSZ fluctuation across the (x, y) angular coordinates, while the right image displays the tSZ Compton parameter. The inner dashed line circle delimits the R_{200} region, while the outer circle marks the boundaries of the high resolution region. In the bottom left corner of the plots, a symbol indicates the direction of the coordinate axis perpendicular to the plane of the sky.

The SZ maps were first converted in grey-scale images, transforming the colour scale from logarithmic in $y_{\rm SZ}$ to linear grey-scale intensity in the $[0, 1]$ interval. The transformation relation is given by

$$y_{\rm kSZ}^{\rm (scaled)} = \frac{a - \log_{10}(|y_{\rm kSZ}|)}{b}, \qquad (29)$$

where the absolute value of $y_{\rm kSZ}$ allows the algorithm to operate in conditions where $y_{\rm kSZ} < 0$. This procedure required the introduction of the conversion coefficients a and b, which were adjusted according to a visual inspection, in order to avoid saturation of bright peaks or excessive darkening of faint signals. Then, subhalos with different sizes were detected by convolving the grey-scaled maps with the LoG method, executed for a range of 80 σ-values and setting an intensity threshold equal to 5% of the maximum value in the map. The lower limit for σ was defined to be the size of the NIKA-2 PSF (i.e. the convolution kernel introduced in the previous section), while the maximum σ was set as R_{200}, compatibly with the size of the ICM.

The result of the LoG-based detection method is shown in figure 9, which marks the position and size of the hot IGM bound to subhalos in the MACSIS cluster 0. The detection procedure was repeated for all clusters in the MACSIS sample, keeping the (a, b) scaling parameters fixed. The fluctuations detected in this process were flagged and included in the *LoG detection catalogue*.

5 Substructure catalogues and detection probabilities

The aim of this work is to estimate the probability of detecting a subhalo with given physical properties from its kSZ signature. In order to obtain such probability distributions, two catalogues have been constructed: the SUBFIND catalogue, generated in the post-processing phase of the MACSIS project, and the LoG detection catalogue, presented in section 4.3. The comparison between the two subhalo catalogues allows to identify the objects with the strongest contribution to the kSZ maps, corresponding also to the most likely ones to be detected. This section explains the matching procedure for the two catalogues, the results deriving from them and the potential implications on observational studies of subhalo IGM using the kSZ effect. A diagram illustrating the work-flow relative to this section is shown in figure 10.

5.1 The SUBFIND selection

The SUBFIND code, run on MACSIS HYDRO data, delivered the catalogue of substructures identified in the simulated galaxy clusters as overdensities with $\mathcal{N} > 20$ dark matter particles (see Dolag et al. 2009, Altamura 2019 and Murin 2019). This limit translates into the SUBFIND mass resolution, which prevents any reliable analysis of subhalos with dark matter mass lower than $2.36 \times 10^{10}\ M_\odot$. In the

$$y_{kSZ}^{(scaled)}$$
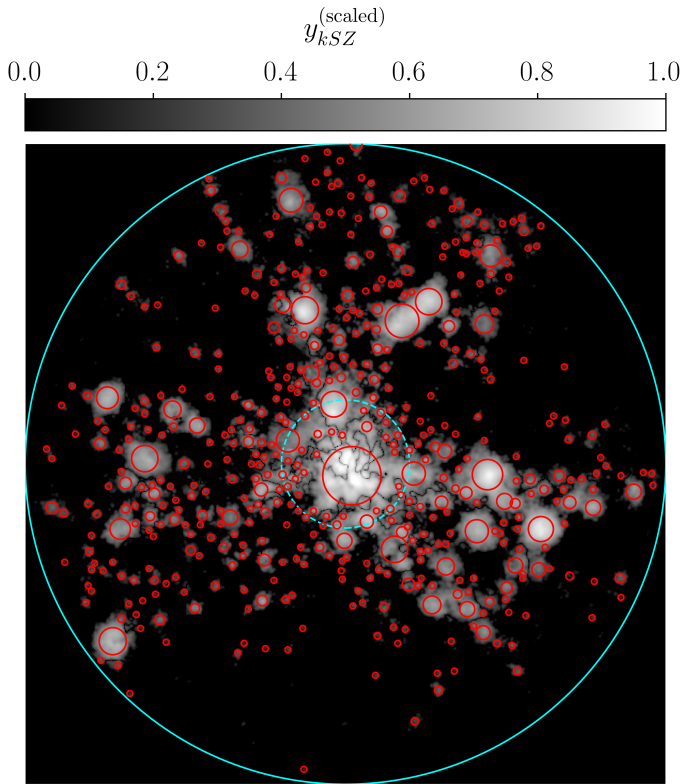
| 0.0 | 0.2 | 0.4 | 0.6 | 0.8 | 1.0 |

Figure 9: Converted grey-scale image from the kSZ relative to the MACSIS halo 0. The red circles mark the positions and sizes of the kSZ fluctuations detected by the LoG algorithm. The outer and inner cyan lines bound the $5 \times R_{200}$ and R_{200} regions respectively. The axes are omitted in this figure, since the LoG method is based on coordinates given by the number of pixels (or bins) in the image.

present work, a more conservative limit was adopted and the analyses were restricted to subhalos with total mass $M > 10^{11}~M_\odot$.

SUBFIND allowed to compute the ratio between the mass M_{gas} of gas particles gravitationally bound to subhalos and their total mass M. This quantity, known as gas fraction, is hence defined as $f_g \equiv M_{gas}/M$ (see e.g. Altamura 2019 and Murin 2019). As shown in Altamura (2019) and Murin (2019), SUBFIND can also be used to trace the exact particles in each subhalo, in order to reconstruct the average bulk motion of the object, expressed by the velocity vector $\mathbf{v}_{sub} \equiv v_x \hat{\mathbf{e}}_x + v_y \hat{\mathbf{e}}_y + v_z \hat{\mathbf{e}}_z$. As in section 4, the LoS component is defined to be in the $\hat{\mathbf{e}}_z$ direction, leading to $v_{\mathrm{LoS}} \equiv v_z$.

Crucially, this step differs from the procedure for re-constructing the kSZ maps: the y_{kSZ} values are computed purely using the velocity information from the individual particles, without the contribution from SUBFIND for determining which ones are self-bound. For this reason, the pipeline dedicated to the analysis of SUBFIND data is deployed with the *a priori* knowledge of the self-boundedness of substructures. Conversely, if such information is not adopted in the analysis, as in section 4.3, the approach is said to be *mock simulation*-based, as labelled in figure 10.

The SUBFIND catalogue provided substructure candidates, which will only be detected by the LoG algorithm if they produce a kSZ signal above the threshold introduced in section 4.3.
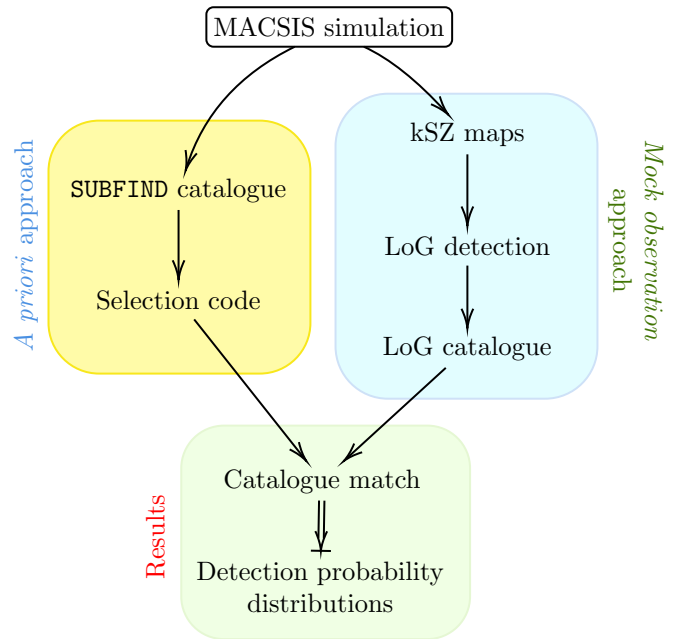

Figure 10: Schematic of the work-flow described in section 5. The yellow box contains illustrated the *a priori* approach, based on the SUBFIND catalogue, while the blue box is dedicated to the *mock observation* approach, based on the LoG detection catalogue. Both are conveyed and compared in the results block, shown in green. Image created using PGF/Ti*kz* modules.

In order to probe in detail the properties of the sub-structure candidates to be matched against the LoG catalogue, a selection filter was developed and deployed in the post-processing pipeline (see appendix A). The selection algorithm has the role of refining the candidates sample, filtering out substructures by f_g, v_z, M and radial distance R from the halo's centre of potential. The selection criteria used in this work can be deduced from figure 11, which reports the number n_{sub} of subhalos, as a function of the quantities stated above. In this work, the selection critera include the lower limit for M, as stated above, as well as $0.03 < R/R_{200} < 5$. The lower limit is given by the *numerical convergence radius*, which represents the spatial resolution associated with the particle ensemble (see e.g. Power et al. 2003, Altamura 2019 and Murin 2019 for detailed description in the context of the MACSIS simulation). As predicted in Altamura (2019) and Murin (2019) with a MACSIS subsample of 10 halos, the majority of the substructures with considerable gas content orbit outside the ICM, whereas subhalos within R_{200} exhibit a drastic decrease of their gas fraction, as a consequence of their hot IGM being stripped by ram pressure.

Figure 11 shows also an anomalous group of subhalos having $f_g \approx 0.12$ and R/R_{200} within 0.07 and 0.5. These objects have been identified to be galaxy clusters with $M \sim 10^{14}~M_\odot$, which interacted with the main ICM, overcome the ram pressure and performed a close encounter with the centre of the larger cluster. Such scenario characterises events of *close merging*, which in the case of MACSIS often involve two large galaxy clusters, although SUBFIND may identify them as subhalos.
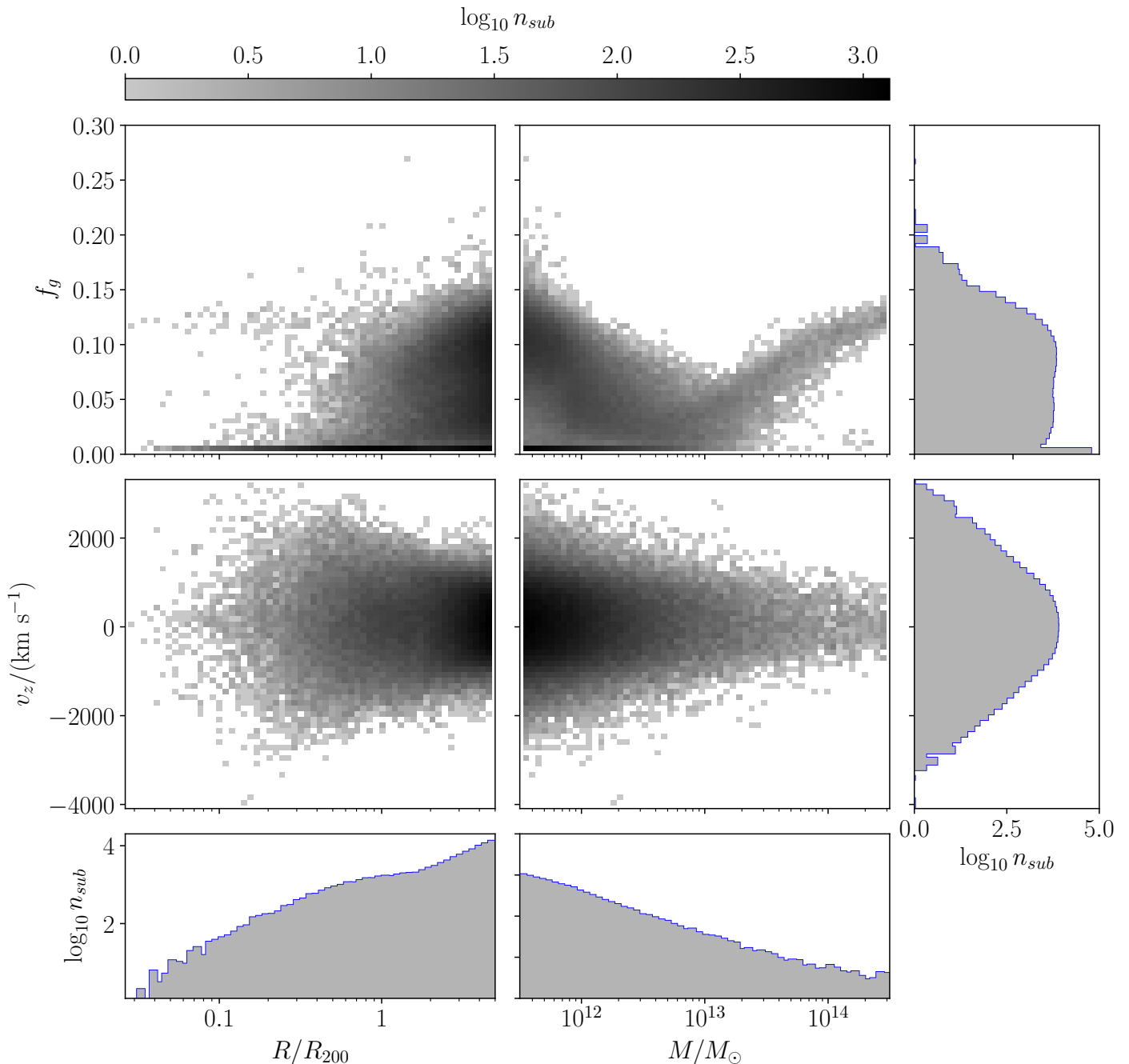
Figure 11: This figure shows the result from the selection operated on the SUBFIND catalogue. The distributions were generated by gathering the subhalo candidates from the 390 MACSIS clusters. The central four plots show the number of subhalos with f_g, v_z, M and R within the corresponding bins, while the two right-most and the bottom plots refer to the marginalised data, calculated by summing the n_{sub} count over rows and columns respectively.

5.2   Matching catalogues

Once obtained the subhalo candidate catalogue from SUBFIND and excluded the objects that did not satisfy the selection critera, the LoG catalogue was conveyed into the last stage of the post-processing pipeline, which involves matching of the two substructure datasets. This procedure associates to each object in the LoG catalogue all the SUBFIND candidates that are located within the boundary of the kSZ peak, as computed through the LoG edge detection. The catalogue matching tool then selects the SUBFIND candidate with the largest mass within each LoG peak and directs it into the final catalogue, containing subhalos with the largest mass, which have also been identified by the LoG method. The result of this procedure is shown in figure 12, where the SUBFIND catalogue is superimposed to the LoG peaks, represented by circles.

By marking the position of the matched subhalos, it is possible to notice that the majority of the large kSZ fluctuations ($y_{kSZ} \sim 10^{-5} - 10^{-6}$) have been correctly identified by the LoG algorithm. However, it has been found that this procedure can lead to inaccuracies in the case of two close-by peaks with comparable intensities. The detection of such features as two separate fluctuations depends upon the threshold value specified in the LoG code, as well as
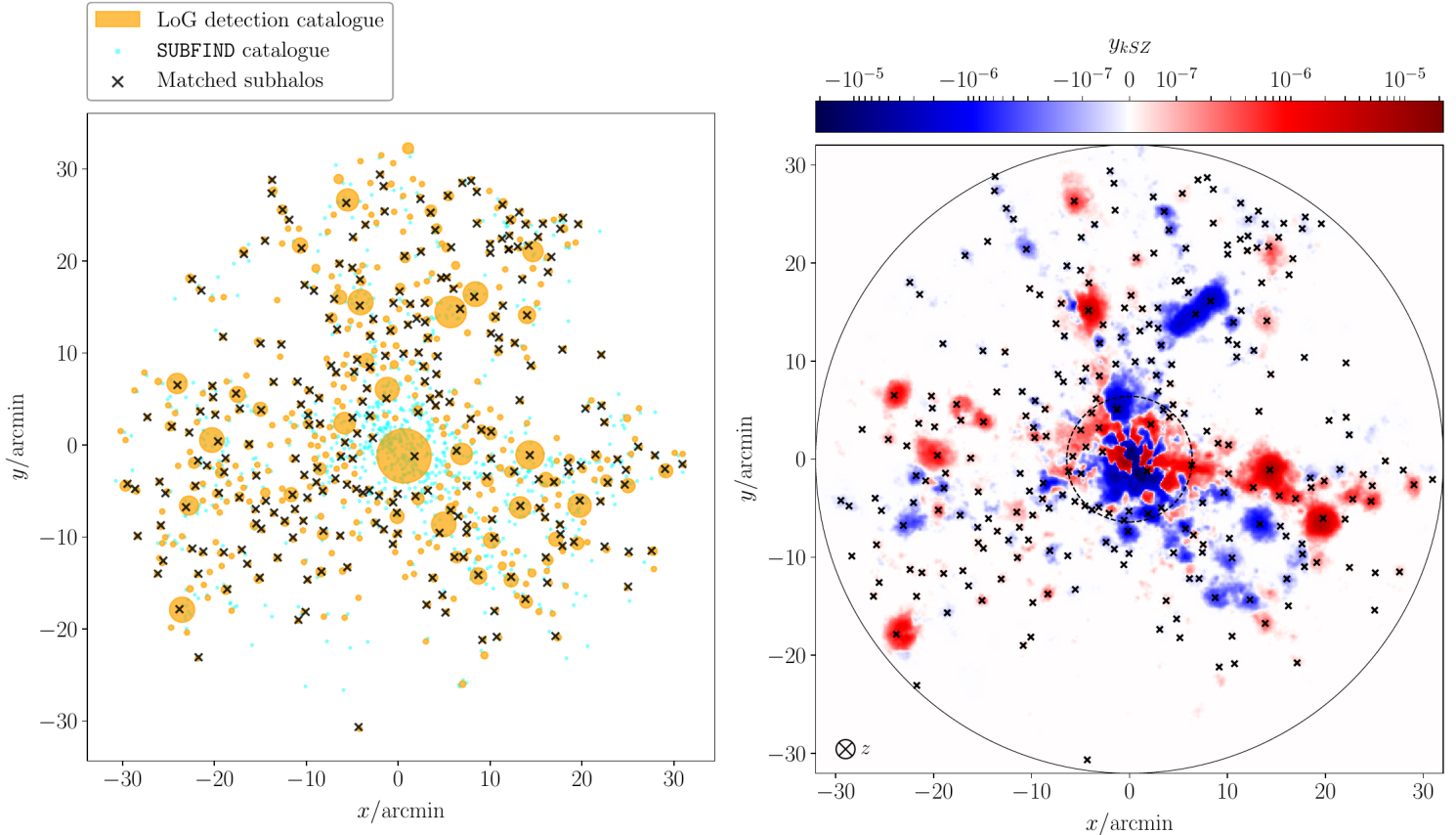
Figure 12: The image on the left shows the filtered `SUBFIND` candidates with light-blue markers, superimposed with the LoG catalogue displayed by the orange circles, relative to the MACSIS halo 0. For each LoG object, the candidate with the largest mass was selected and shown by a black marker. These subhalos constitute the resulting matched catalogue. On the right, the positions of matched `SUBFIND` candidates are indicated in the relative kSZ map using black crossed markers.

the choice of grey-scale conversion parameters (a, b).

Furthermore, numerous matched candidates have been detected within the R_{200} region, apparently contradicting the hypothesis advanced in the previous section, regarding a lack of substructures with enough self-bound gas to produce a detection. In order to investigate this peculiarity, the `SUBFIND` catalogue has been processed using the selection algorithm, which filtered out all the substructures outside the R_{200} sphere. As expected, the result showed very few substructures having low f_g and which are not individually detected by the LoG algorithm. The substructures that appear to lie within the R_{200} sphere in fact orbit outside the virial radius, along the same LoS of the ICM.

As in previous sections, the study of matched subhalos was repeated for the 390 clusters in the MACSIS sample. At the end of the process, the catalogue with matched substructures contained the properties of all the objects that have been detected.

5.3 Observability analysis

The catalogue of matched substructures allowed to find the f_g, v_z, M and R values of the most massive subhalos within each detected peak. The comparison with the output from the `SUBFIND` algorithm (see figure 11) can therefore be performed by considering the ratio n^*/n_{sub}, where n^* is the

number of subhalos detected with the LoG algorithm and matched to the `SUBFIND` candidates and n_{sub} is the total number of `SUBFIND` candidates.

According to the frequentist interpretation of statistical probabilities, the n^*/n_{sub} ratio estimates the probability that a subhalo, with given f_g, v_z, M and R values, can be detected using the LoG detection algorithm. Provided that the statistical sample used to generate the probability distribution is large, the ratio can be regarded as a reliable indicator for the corresponding probability. The pipeline deployed for the post-processing of MACSIS data allowed to combine the catalogues containing the `SUBFIND` candidates and the LoG detections for 390 clusters, resulting in the plots shown in figure 13.

The analysis of the probability distributions for (R, f_g) and (R, v_z) indicate that a significant fraction of subhalos within he virial radius have not been detected. This effect is primarily due to their low gas fraction, which prevents the generation of detectable kSZ signals. Secondly, the detection of faint kSZ fluctuations in the vicinity of a larger sources of signal, such as the ICM, is found to introduce a bias in the output, as the LoG algorithm is not optimised for handling the processing of similar images. As noted in previous sections, the subgroups identified as close mergers exhibit a high detection rate, motivated by their mass and their significant gas fraction. Ultimately, the marginal
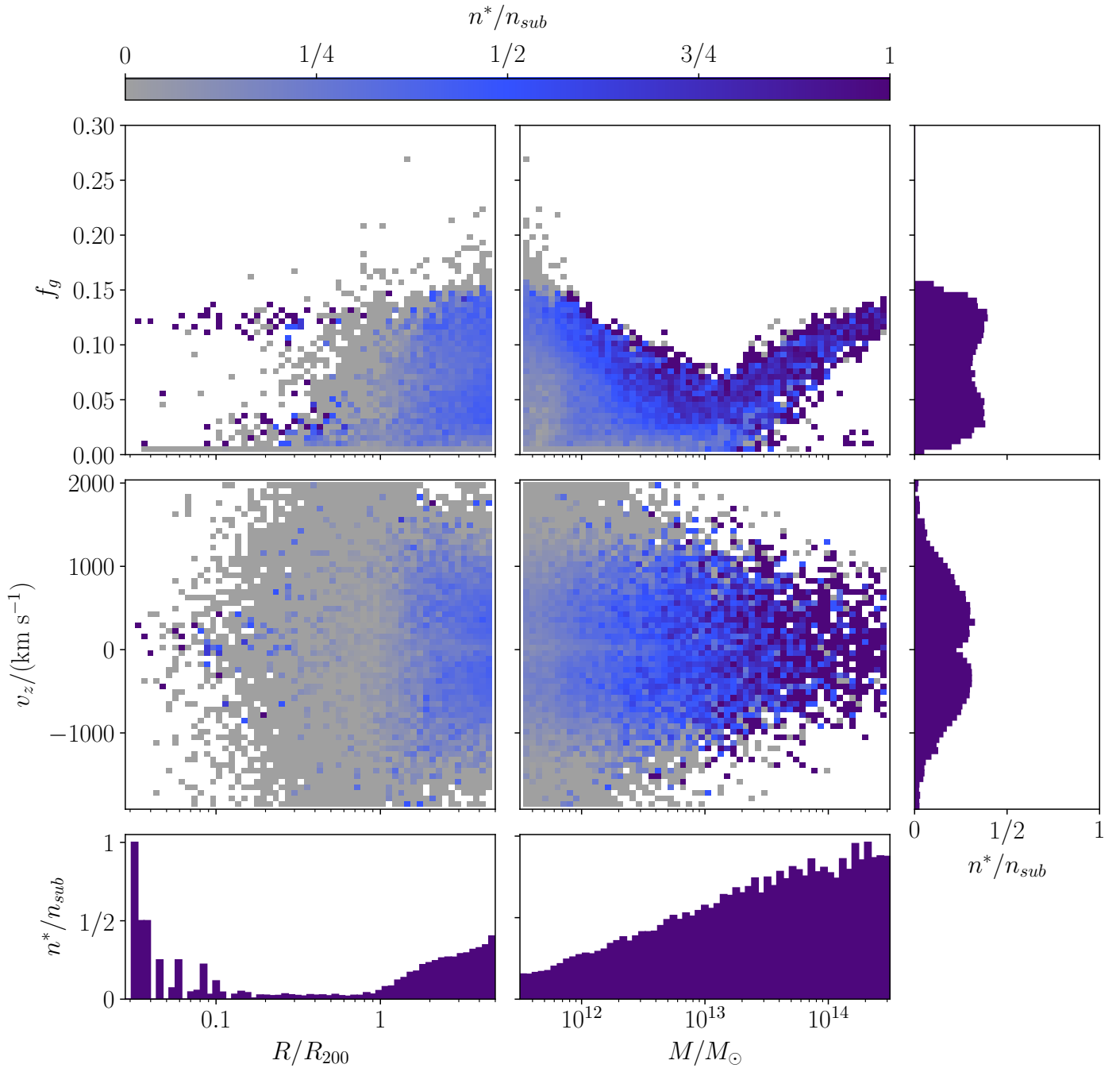
Figure 13: Probability distributions relative to the detectability of subhalo IGM through the kSZ effect, simulated at the NIKA-s resolution. The plots result from the combination of 390 galaxy clusters in the MACSIS sample, simulated at redshift $z = 0.57$. The four central plots represent the probability distributions linking the subhalo parameters introduced in figure 11, while the right-most and bottom plots show the marginal probabilities drawn from the central plots. The white regions indicate absence of subhalos, both in the SUBFIND catalogue and in the LoG catalogue. The grey bins represent the SUBFIND objects not being detected, hence leading to $n^*/n_{sub} = 0$. The blue colour coding traces instead an increasingly high frequency of detected subhalos, which are also matched to the SUBFIND catalogue. Ultimately, the purple colour is assigned to the detections that uniquely correspond to a single SUBFIND subhalo.

distribution $(R, n^*/n_{sub}$ clearly shows that substructures within the ICM can be detected with $< 5\%$ probability on average, while outside the virial sphere the detection rate increases up to $\approx 41\%$. The large values at $R \lesssim 0.1 \times R_{200}$ are also characterised by a considerable scatter, largely attributed to the contribution of the close mergers and the Poisson noise deriving from the scarce statistical sample.

The (M, f_g) distribution shows an approximately lin-

ear relation between $\log_{10} M$ and f_g for $M \gtrsim 10^{13} M_\odot$, which has been highlighted in previous studies involving the MACSIS simulation (Altamura, 2019; Murin, 2019). The subhalos appearing in this region are both orbiting outside the virial sphere and have a mass comparable to that of small galaxy clusters. As a consequence, their IGM is less exposed to ram pressure and tidal stripping, which leads to a high probability of producing measurable

kSZ signals. On the other hand, the collisional nature of the subhalo IGM can be deduced by the behaviour of the (M, f_g) distribution for $10^{11} M_\odot \lesssim M \lesssim 10^{13} M_\odot$. The large scatter in the distribution of f_g values is a consequence of the stripping, which causes small galaxy groups to loose gas and leading to the high number of subhalos with $f_g \approx 0$. Although those substructures cannot be observed through the kSZ effect, a group of objects with comparable mass to those affected by gas stripping is found to have a gas fraction $f_g \gtrsim 0.08$. As shown in figure 13, these subhalos are distributed along the upper envelope of the (M, f_g) diagram and can reach detection rates between 75% and 90%, provided that the the instrument used to conduct the observation is sensitive enough to reconstruct their small y_{kSZ} parameter.

The (M, v_z) distribution, in conjunction with its associated marginal probabilities, is likely to be one of the most relevant results presented in this work for the reconstruction of substructure velocity fields from kSZ observations. As expected from the complementary distributions in figure 13, the wide grey area at low masses reflects the abundance of small-scale undetected subhalos with little to no self-bound hot gas. However, the n^*/n_{sub} ratio is observed to decrease also in the region close to $|v_z| \approx 0$, with $0 \lesssim n^*/n_{sub} \lesssim 0.25$. As introduced in section 2.3, the substructures with low values of the line of sight velocity $v_{\text{LoS}} \equiv v_z$ are not expected to contribute to the kSZ signal.

The substructures with $M \gtrsim 10^{13} M_\odot$ constitute an exception. In spite of the low v_z, their mass might be sufficient to generate a detectable kSZ distortion, as can be explained by considering the argument of the summation in equation 26. A different hypothesis contemplates the possibility that the large substructures with low LoS velocity may be geometrically aligned with independent (smaller) substructures which are moving faster. In such scenario, the LoG algorithm is expected to detect one single fluctuation in the kSZ map; the procedure for matching catalogues would then select the most massive object identified within the boundaries of the kSZ peak, leading the smaller and faster substructure to be ignored by the pipeline, in favour of the larger stationary object in the background. This consideration highlights one of the limitations of the LoG algorithm, which causes a degree of confusion in the case of multiple aligned subhalos and therefore a bias towards high-mass substructures.

The low detection rate in correspondence of $v_z = 0$ can be also observed in the marginal displaying n^*/n_{sub} as a function of v_z. Assuming that the hypothesis regarding the high-mass bias is valid, the central part of the marginal plot suggests that its contribution to the subhalos with small LoS velocity is $\approx 20\%$, in contrast with the expectation from equation 26, which predicts $n^*/n_{sub} \to 0$ as $|v_z| \to 0$. In addition, the present study found that repeating the analysis by calculating the subhalo velocities in the CMB rest frame, rather than the clusters' rest frame, leads to an increase in mass bias (see appendix C). This effect will be the subject of upcoming works, which will target different detection methods and upgraded versions of the post-processing pipeline.

Lastly, the marginal showing n^*/n_{sub} as a function of M simply suggests that low-mass galaxy groups can be de-

tected through the kSZ are less likely to be detected, in comparison with larger subhalos. The detection rates in this case range from $\approx 20\% - 90\%$. In-depth studies of the shape of this distribution will also be included in the future development of this project.

The relevance of the results presented in figure 13 is deeply connected to the probability of observing a kSZ fluctuation in a real observation. In their study about the kSZ substructure in MACS J0717.5+3745, Adam et al. (2017) noted how the calibration and data reduction methods used is highly dependent on the likelihood model assumed. As a result of the inaccuracies in estimating the uncertainties, they found that Monte-Carlo Markov-Chain (MCMC) methods are unable to provide reliable results for fluctuations close to the noise level $(1 - 2\sigma)$. If estimates for the mass and gas content of a particular galaxy clusters are available from independent observations (e.g. weak lensing and X-ray emission), then it would possible to infer the *a priori* probability that a substructure will be detected from the n^*/n_{sub} distributions in figure 13. This probability estimate, constructed using the MACSIS simulation, could therefore guide the definition of more accurate likelihood models to implement into MCMC pipelines for the analysis of kSZ observations.

6 Summary and future work

The Sunyaev-Zel'dovich effect is one of the main parts of the phenomenology related to galaxy clusters. It is generated by the comptonisation of CMB photons due to high energy electrons in the IGM of galaxy clusters. The resulting spectral distortion can be due to the temperature distribution of the ionised plasma gravitationally bound to galaxy clusters (tSZ) or due to the bulk motion of galaxy clusters and their substructure with respect to the CMB rest frame (kSZ). The main focus of this work involved the study of kSZ signals generated by cluster substructure moving with respect to the rest frame of the cluster. Considering substructures with a given mass, velocity and gas content, the final goal of the project is to estimate the probability for such objects to produce a detectable kSZ signal.

In order to conduct this study, the MACSIS simulation was analysed using a pipeline developed by the author, in partnership with a project collaborator (Barnes et al., 2015, 2017; Altamura, 2019; Murin, 2019). The post-processing followed two independent approaches. The *a priori* approach consisted in retrieving the output data from the SUBFIND code (Springel et al., 2001b), which was run on the MACSIS clusters with the aim of identifying local overdensities of 20 or more particles. The SUBFIND catalogue was then completed by calculating the gas fraction, distance from the centre of the main halo and average bulk velocity for each subhalo. This ensemble of substructures was filtered using a selection algorithm that retains only the substructures with gas fractions, radial distance and LoS velocity within specified values. The result of the selection procedure was s list of subhalos proposed as candidates for the catalogue matching stage.

The *mock observation* approach is the second post-

processing route that has been used in the present study. It is independent of the SUBFIND data and is solely based on the physical properties of the single gas particles in the MACSIS HYDRO halos. The post-processing pipeline was used to compute the kSZ maps for the 390 clusters in the simulation. The kSZ maps were then analysed using the Laplacian of Gaussians (LoG) algorithm, detected the fluctuations based on grey-scaled kSZ maps (Gonzalez et al., 2009; Powell et al., 2009). This procedure resulted in the LoG catalogue, which contains the position of the centroid and the size of each detected fluctuation.

Ultimately, the SUBFIND candidates were matched to the LoG catalogue: for each detected peak, the pipeline flagged the subhalo with the largest mass located within the boundaries of the kSZ fluctuation. This class of subhalos forms the detected (or matched) subhalos and constitutes a subset of the SUBFIND catalogue after the first selection step. The ratio between the number of detected subhalos and the total number of potential candidates gives the detection rate, which expressed the (frequentist) probability that a substructure with given properties (see figure 13) can be detected with an algorithm analogous to the LoG method (Gonzalez et al., 2009; Powell et al., 2009).

This result has the potential to provide *a priori* likelihood estimates on the observability of galaxy cluster substructures through the kSZ effect, as a function of their spatial position, kinematics and baryonic composition. Consequently, the present work can suggest likelihood models for reducing data from microwave observation tailored towards the detection of the kSZ effect with NIKA-like facilities (e.g. Adam et al. 2017). As noted in section 5, the method illustrated in this analysis presents limitations, which may introduce biases in the prediction for the detectability rates. In particular, the distribution of n^*/n_{sun} against v_z suggests the action of a bias towards substructures with masses $M \gtrsim 10^{13} M_\odot$. Further developments of this project may therefore involve a detailed analysis with the aim of confirming or refuting the presence of a high-mass bias. Moreover, the deployment of peak detection algorithms with adaptive local estimators may contribute in identifying closely located fluctuations, avoiding the saturation of the grey-scale images and improving the statistical significance of the final outcomes.

Acknowledgements and contributions

References

Adam R., et al., 2014, Astronomy and Astrophysics, 569, A66

Adam R., et al., 2016, Astronomy and Astrophysics, 586, A122

Adam R., et al., 2017, Astronomy and Astrophysics, 598, A115

Allen S. W., Evrard A. E., Mantz A. B., 2011, Annual Review of Astronomy and Astrophysics, 49, 409

Altamura E., 2019, Substructures in the MACSIS hydrodynamical simulation of galaxy clusters, MPhys Thesis, https://github.com/edoaltamura/MPhys_thesis

Arons J., Silk J., 1968, Monthly Notices of the RAS, 140, 331

Bahé Y. M., McCarthy I. G., Crain R. A., Theuns T., 2012, Monthly Notices of the Royal Astronomical Society, 424, 1179

Baldi A. S., De Petris M., Sembolini F., Yepes G., Cui W., Lamagna L., 2018, Monthly Notices of the RAS, 479, 4028

Barnes D. J., Henson M. A., Kay S. T., McCarthy I. G., Bahe Y. M., Eagle Collaboration 2015, in Exploring the Hot and Energetic Universe: The first scientific conference dedicated to the Athena X-ray observatory. p. 41

Barnes D. J., Kay S. T., Henson M. A., McCarthy I. G., Schaye J., Jenkins A., 2017, Monthly Notices of the RAS, 465, 213

Basu K., Sommer M., Erler J., Eckert D., Vazza F., Magnelli B., Bertoldi F., Tozzi P., 2016, The Messenger, 166, 53

Basu K., et al., 2019, arXiv e-prints,

Baxter E. J., Sherwin B. D., Raghunathan S., 2019, arXiv e-prints, p. arXiv:1904.04199

Binney J., Tremaine S., 1987, Galactic dynamics

Birkinshaw M., 1999, Physics Reports, 310, 97

Birkinshaw M., Gull S. F., Northover K. J. E., 1978, Monthly Notices of the RAS, 185, 245

Blumenthal G. R., Faber S. M., Primack J. R., Rees M. J., 1984, Nature, 311, 517

Bond J. R., Cole S., Efstathiou G., Kaiser N., 1991, Astrophysical Journal, 379, 440

Booth C. M., Schaye J., 2009, Monthly Notices of the RAS, 398, 53

Bower R. G., 1991, Monthly Notices of the RAS, 248, 332

Byram E. T., Chubb T. A., Friedman H., 1966, Science, 152, 66

Carlstrom J. E., Joy M., Grego L., 1996, Astrophysical Journal, 456, L75

Carlstrom J. E., Holder G. P., Reese E. D., 2002, Annual Review of Astronomy and Astrophysics, 40, 643

Catalano A., et al., 2018, Journal of Low Temperature Physics, 193, 916

Chen J.-S., Huertas A., Medioni G., 1987, IEEE Transactions on Pattern Analysis and Machine Intelligence, pp 584–590

Chluba J., Mannheim K., 2002, Astronomy and Astrophysics, 396, 419

Chluba J., Sunyaev R. A., 2004, Astronomy and Astrophysics, 424, 389

Chluba J., Nagai D., Sazonov S., Nelson K., 2012, Monthly Notices of the RAS, 426, 510

Cole S., Lacey C. G., Baugh C. M., Frenk C. S., 2000, Monthly Notices of the RAS, 319, 168

Conselice C. J., Bluck A. F. L., Mortlock A., Palamara D., Benson A. J., 2014, Monthly Notices of the RAS, 444, 1125

Dalla Vecchia C., Schaye J., 2012, Monthly Notices of the RAS, 426, 140

Davé R., et al., 2001, Astrophysical Journal, 552, 473

Davis M., Efstathiou G., Frenk C. S., White S. D. M., 1985, Astrophysical Journal, 292, 371

De Lucia G., Kauffmann G., Springel V., White S. D. M., Lanzoni B., Stoehr F., Tormen G., Yoshida N., 2004, Monthly Notices of the RAS, 348, 333

Diaferio A., Schindler S., Dolag K., 2008, Space Science Reviews, 134, 7

Diemand J., Moore B., Stadel J., 2004, Monthly Notices of the RAS, 352, 535

Dolag K., Borgani S., Murante G., Springel V., 2009, Monthly Notices of the RAS, 399, 497

Dressler A., Shectman S. A., 1988, Astronomical Journal, 95, 985

Fisenko A. I., Lemberg V. F., 2018, Astrophysics and Space Science, 363, 224

Gao L., De Lucia G., White S. D. M., Jenkins A., 2004, Monthly Notices of the RAS, 352, L1

Geller M. J., Beers T. C., 1982, Publications of the ASP, 94, 421

Ghigna S., Moore B., Governato F., Lake G., Quinn T., Stadel J., 2000, Astrophysical Journal, 544, 616

Gill S. P. D., Knebe A., Gibson B. K., 2005, Monthly Notices of the RAS, 356, 1327

Gnedin N. Y., Hui L., 1998, Monthly Notices of the RAS, 296, 44

Gonzalez R. C., Woods R. E., Eddins S. L., et al., 2009, Publisher T. Robbins, Printed in USA, 11, 531

Grainge K., Jones M., Pooley G., Saunders R., Edge A., 1993, Monthly Notices of the RAS, 265, L57

Henson M. A., Barnes D. J., Kay S. T., McCarthy I. G., Schaye J., 2017, Monthly Notices of the RAS, 465, 3361

Illarionov A. F., Syunyaev R. A., 1972, Soviet Astronomy, 16, 45

Jauch J. M., Rohrlich F., 1976, The theory of photons and electrons. The relativistic quantum field theory of charged particles with spin one-half

Jauzac M., et al., 2018, Monthly Notices of the RAS, 481, 2901

Jenkins A., 2010, Monthly Notices of the RAS, 403, 1859

Jenkins A., 2013, Monthly Notices of the RAS, 434, 2094

Jenkins A., Booth S., 2013, arXiv e-prints, p. arXiv:1306.5771

Jones M., et al., 1993, Nature, 365, 320

Kauffmann G., White S. D. M., 1993, Monthly Notices of the RAS, 261, 921

Kompaneets A., 1956, Zh. Eksp. Teor. Fiz, 31, 876

Kong H., Akakin H. C., Sarma S. E., 2013, IEEE transactions on cybernetics, 43, 1719

Kravtsov A. V., Borgani S., 2012, Annual Review of Astronomy and Astrophysics, 50, 353

Kravtsov A. V., Berlind A. A., Wechsler R. H., Klypin A. A., Gottlöber S., Allgood B. o., Primack J. R., 2004, Astrophysical Journal, 609, 35

Lacey C., Cole S., 1993, Monthly Notices of the RAS, 262, 627

Lightman A. P., Rybicki G. B., 1979a, in Bulletin of the AAS. p. 793

Lightman A. P., Rybicki G. B., 1979b, Astrophysical Journal, 232, 882

Lightman A. P., Rybicki G. B., 1980, Astrophysical Journal, 236, 928

Limousin M., et al., 2012, Astronomy and Astrophysics, 544, A71

Limousin M., et al., 2016, Astronomy and Astrophysics, 588, A99

Ma C.-J., Ebeling H., Barrett E., 2009, Astrophysical Journal, Letters, 693, L56

Mason B. S., et al., 2010, Astrophysical Journal, 716, 739

McCarthy I. G., Frenk C. S., Font A. S., Lacey C. G., Bower R. G., Mitchell N. L., Balogh M. L., Theuns T., 2008, Monthly Notices of the RAS, 383, 593

McCarthy I. G., Schaye J., Bird S., Le Brun A. M. C., 2017, Monthly Notices of the RAS, 465, 2936

Merluzzi P., et al., 2015, Monthly Notices of the RAS, 446, 803

Moffet A. T., Birkinshaw M., 1989, Astronomical Journal, 98, 1148

Moore B., Ghigna S., Governato F., Lake G., Quinn T., Stadel J., Tozzi P., 1999, Astrophysical Journal, 524, L19

Mroczkowski T., et al., 2012, Astrophysical Journal, 761, 47

Mroczkowski T., et al., 2019, Space Science Reviews, 215, 17

Murin M., 2019, Substructures in the MACSIS hydrodynamical simulation of galaxy clusters, MPhys Thesis

Nagai D., Lau E. T., 2011, Astrophysical Journal, 731, L10

Pariiskii Y. N., 1973, Soviet Astronomy, 16, 1048

Peacock J. A., 1999, Cosmological Physics

Perrott Y. C., Javid K., Carvalho P., Elwood P. J., Hobson M. P., Lasenby A. N., Olamaie M., Saunders R. D. E., 2019, Monthly Notices of the RAS, 486, 2116

Planck Collaboration et al., 2016a, Astronomy and Astrophysics, 586, A139

Planck Collaboration et al., 2016b, Astronomy and Astrophysics, 594, A27

Porter S. C., Raychaudhury S., 2005, Monthly Notices of the RAS, 364, 1387

Powell L. C., Kay S. T., Babul A., 2009, Monthly Notices of the RAS, 400, 705

Power C., Navarro J. F., Jenkins A., Frenk C. S., White S. D. M., Springel V., Stadel J., Quinn T., 2003, Monthly Notices of the RAS, 338, 14

Press W. H., Schechter P., 1974, Astrophysical Journal, 187, 425

Prigogine I., Geheniau J., Gunzig E., Nardone P., 1989, General Relativity and Gravitation, 21, 767

Raymond J. C., Smith B. W., 1977, Astrophysical Journal, Supplement, 35, 419

Renzini A., 2004, in Mulchaey J. S., Dressler A., Oemler A., eds, Clusters of Galaxies: Probes of Cosmological Structure and Galaxy Evolution. p. 260 (arXiv:astro-ph/0307146)

Rogers F. J., Swenson F. J., Iglesias C. A., 1996, Astrophysical Journal, 456, 902

Ruan J. J., Quinn T. R., Babul A., 2013, Monthly Notices of the RAS, 432, 3508

Rybicki G. B., Lightman A. P., 1979, Radiative LoS in astrophysics

Sarazin C. L., 1986, Reviews of Modern Physics, 58, 1

Sarazin C. L., 2002, in Feretti L., Gioia I. M., Giovannini G., eds, Astrophysics and Space Science Library Vol. 272, Merging LoS in Galaxy Clusters. pp 1–38 (arXiv:astro-ph/0105418), doi:10.1007/0-306-48096-4˙1

Sayers J., et al., 2013, Astrophysical Journal, 778, 52

Schaye J., et al., 2010, Monthly Notices of the RAS, 402, 1536

Springel V., 2005, Monthly Notices of the RAS, 364, 1105

Springel V., Yoshida N., White S. D. M., 2001a, New Astronomy, 6, 79

Springel V., White S. D. M., Tormen G., Kauffmann G., 2001b, Monthly Notices of the RAS, 328, 726

Stebbins A., 2007, arXiv e-prints, pp astro–ph/0703541

Sunyaev R. A., Khatri R., 2013, Journal of Cosmology and Astro-Particle Physics, 2013, 012

Sunyaev R. A., Zeldovich Y. B., 1969, Nature, 223, 721

Sunyaev R. A., Zeldovich Y. B., 1970a, Comments on Astrophysics and Space Physics, 2, 66

Sunyaev R. A., Zeldovich Y. B., 1970b, Astrophysics and Space Science, 7, 3

Sunyaev R. A., Zeldovich Y. B., 1970c, Astrophysics and Space Science, 7, 20

Sunyaev R. A., Zeldovich Y. B., 1972, Comments on Astrophysics and Space Physics, 4, 173

Sunyaev R. A., Zeldovich I. B., 1980, Annual Review of Astronomy and Astrophysics, 18, 537

Takizawa M., 2005, Astrophysical Journal, 629, 791

Tonnesen S., Bryan G. L., 2008, Astrophysical Journal, 684, L9

Tweed D. P., Mamon G. A., Thuan T. X., Cattaneo A., Dekel A., Menci N., Calura F., Silk J., 2018, Monthly Notices of the RAS, 477, 1427

Valageas P., Schaeffer R., Silk J., 2002, Astronomy and Astrophysics, 388, 741

Walker S. A., et al., 2019a, arXiv e-prints, p. arXiv:1903.04550

Walker S., et al., 2019b, Space Science Reviews, 215, 7

Weinberg D. H., Mortonson M. J., Eisenstein D. J., Hirata C., Riess A. G., Rozo E., 2013, Physics Reports, 530, 87

West M. J., Jones C., Forman W., 1995, Astrophysical Journal, 451, L5

White S. D. M., Frenk C. S., 1991, Astrophysical Journal, 379, 52

Zeldovich Y. B., Sunyaev R. A., 1969, Astrophysics and Space Science, 4, 301

Zemcov M., et al., 2010, Astronomy and Astrophysics, 518, L16

Zwicky F., 1951, Publications of the ASP, 63, 61

da Silva A. C., Barbosa D., Liddle A. R., Thomas P. A., 2000, Monthly Notices of the RAS, 317, 37

da Silva A. C., Barbosa D., Liddle A. R., Thomas P. A., 2001a, Monthly Notices of the RAS, 326, 155

da Silva A. C., Kay S. T., Liddle A. R., Thomas P. A., Pearce F. R., Barbosa D., 2001b, Astrophysical Journal, 561, L15

Appendix A   Post-processing the MACSIS simulation: software architecture

The study presented in this report was conducted using a post-processing pipeline developed by the author, together with project collaborators. The main programming language used was `Python-3`, although Wolfram Mathematica 11 and Adobe Photoshop CC played an important role in the grey-scale conversion for the detection of subhalos in SZ maps. Figure 14 shows the call hierarchy of the custom modules with the highest usage. The graph was generated after running the `cprofile` module on the code used to generate the final result, presented in section 5. For this reason, figure 14 does not represent an exhaustive list of the entire framework developed for the analysis of MACSIS data. Intermediate files, which do not directly enter the call history of `map_kSZ_substructure_match.py`, are not explicitly linked to the active ones, but assisted the correct execution of the main pipeline at runtime. Examples of such codes include the organisation and sorting tools (written in `Python-2.7`) for retrieving the MACSIS data from a central Network Attached Storage (NAS) unit and arranging them in a directory hierarchy compatible with `clusters_retriever.py`.

After the formatting and organisation of the data operated by `clusters_retriever.py`, `distance_cosmology.py` computes the angular diameter distance of the MACSIS cluster at the given redshift, in synergy with `cluster_profiler.py`, which deploys the subhalo and particle physical quantities as usable `numpy.arrays`. This file also contains methods for an initial diagnostic test on the cluster properties, such as computing the cluster's rest frame and converting the data from co-moving coordinates into physical (and vice-versa). `kernel_convolver.py` is instead an `astropy`-based tool for the definition of convolution kernels used throughout the pipeline, including the NIKA-2 PSF kernel and the multi-frequency Planck-HFI PSF (omitted in the final presentation of this work). The upper level includes the `map_renderer_SZ.py` module, which is based on lower-level dependencies and contains methods for the generation of SZ maps in a systematic and user-friendly way. Furthermore, it provides the input data for `bloblog_sub_id.py`, dedicated to the feature detection using the Laplacian of Gaussians method. `bloblog_sub_id.py` then returns the catalogue of the detected subhalos, including the centroid position on the maps and their radial extent, in units of image pixels. The independent subhalo catalogue from `SUBFIND` was then handled by the `subhalo_marker.py` code, which associates to each subhalo a *marker*-class object. These objects are then filtered according to five parameters by `gas_fractions_gridSpec_calculator.py` and `subhalo_selection.py`.

The filtered catalogue from `SUBFIND` was ultimately conveyed into `catalogue_compare.py`, which allowed to correlate it with the output from the feature detection algorithm. The merged master catalogue includes the most massive subhalos that are also detected by `bloblog_sub_id.py` and is further analysed and rendered using the `map_kSZ_substructure_match.py` code and definitions in `map_plot_parameters.py`.

Appendix B   Rotation of galaxy clusters

The kSZ spectral distortion in the spectrum of the CMB due to the IGM of a galaxy cluster can be decomposed into several components. Firstly, the bulk translational motion of the cluster in the CMB rest frame will be observed as a monopole contribution, which is expected to trace the overall distribution of the IGM. In addition to the monopole-like contribution, a dipole kSZ distortion can be present and can be associates to the bulk rotation of the galaxy cluster. This phenomenon is known in the literature as the *rotational* kinematic Sunyaev-Zel'dovich (rkSZ) effect and its contribution to the y_{kSZ} parameter is expected to be very small, given the very low spin-parameter associated with galaxy clusters predicted by the ΛCDM model. Over the last two decades, the research involving the rkSZ effect have been limited to analytical/semi-analytical models (see e.g. Chluba & Mannheim (2002)) and results from hydrodynamical simulations (Baldi et al., 2018). However, a recent study, performed by Baxter et al. (2019), claims the detection (2σ) of the rkSZ signal by combining data from the Sloan Digital Sky Survey (SDSS) and the Planck SZ clusters catalogue.
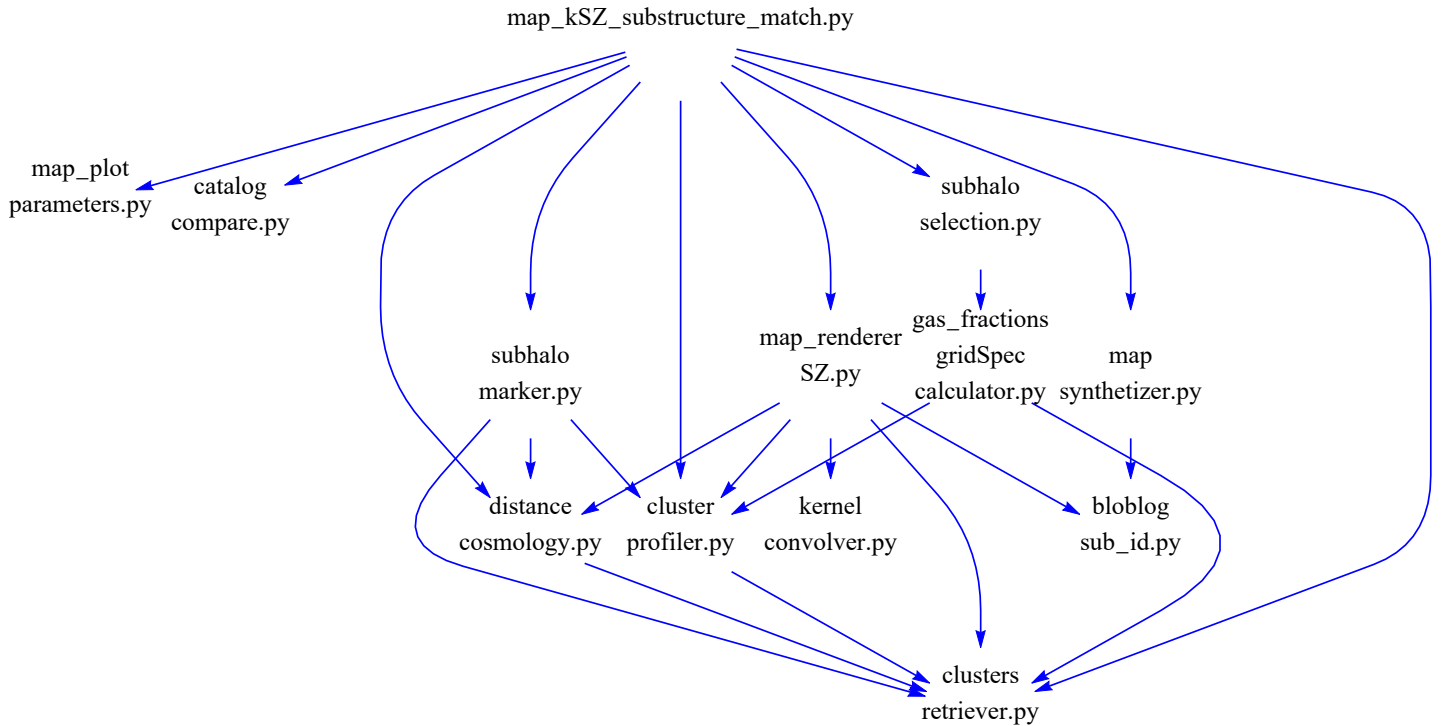
Figure 14: Graph showing the call hierarchy of the `map_kSZ_substructure_match.py` code, used for the generation of the final results presented in this work. The top of the graph represents the highest levels of the pipeline hierarchy, while the lower sectors constitute a closer interface to the MACSIS data, obtained through `clusters_retriever.py`. The call structure was generated using the `cprofile` tools and a PyCharm interface. The graph data were then analysed and rendered in Wolfram Mathematica 11.
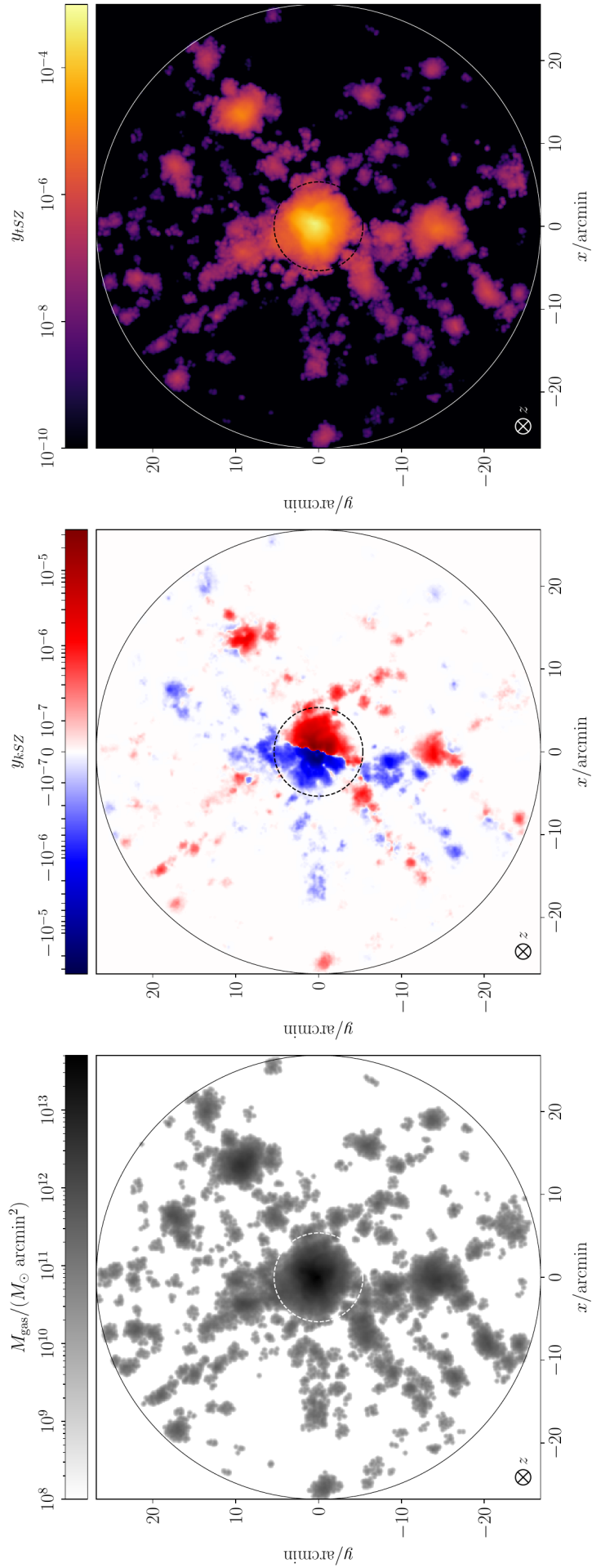
This appendix contains the mass and SZ maps of two selected MACSIS clusters, which exhibit a dipole pattern in the simulated kSZ signal. Figures 15 and 16 show a visible kSZ distribution (in the clusters' rest frames) that clearly suggests the presence of a bulk rotation of the ICM. The colour coding suggests values of $y_{kSZ} \sim 10^{-7}$, which indicate an extremely small distortion of the CMB spectrum, here enhanced by the use of a symmetric-logarithmic colour map.

As noted by Baxter et al. (2019), such small contributions to the overall SZ effect can be revealed by stacking the signals from an ensemble of galaxy clusters, for which independent measurements determined the orientation of their axis of rotation.

Appendix C   kSZ observability of subhalos in the CMB rest frame

As explained in appendix B, the kSZ signal can be decomposed into the bulk motion monopole and higher order contributions. The present study using the MACSIS simulation has found that the inclusion of the bulk velocity of the galaxy clusters affects the detection of the subhalos. The probability distributions relative to the detection of the subhalo IGM fluctuations can be observed in figure 17.

A detailed analysis of these results will be the subject of future work and will be described in a follow-up document.

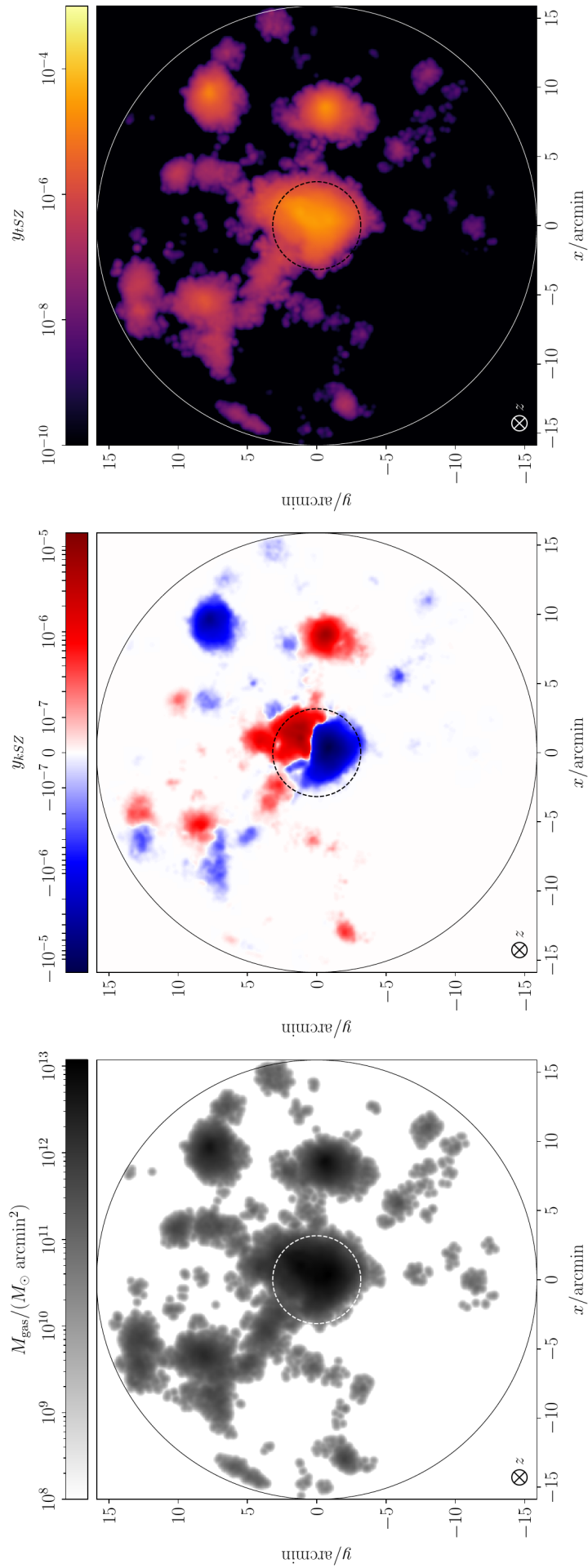Figure 15: Mass and SZ maps relative to the MACSIS halo 49, displayed with a $5 \times R_{200}$ field of view.

Figure 16: Mass and SZ maps relative to the MACSIS halo 7, displayed with a $5 \times R_{200}$ field of view.
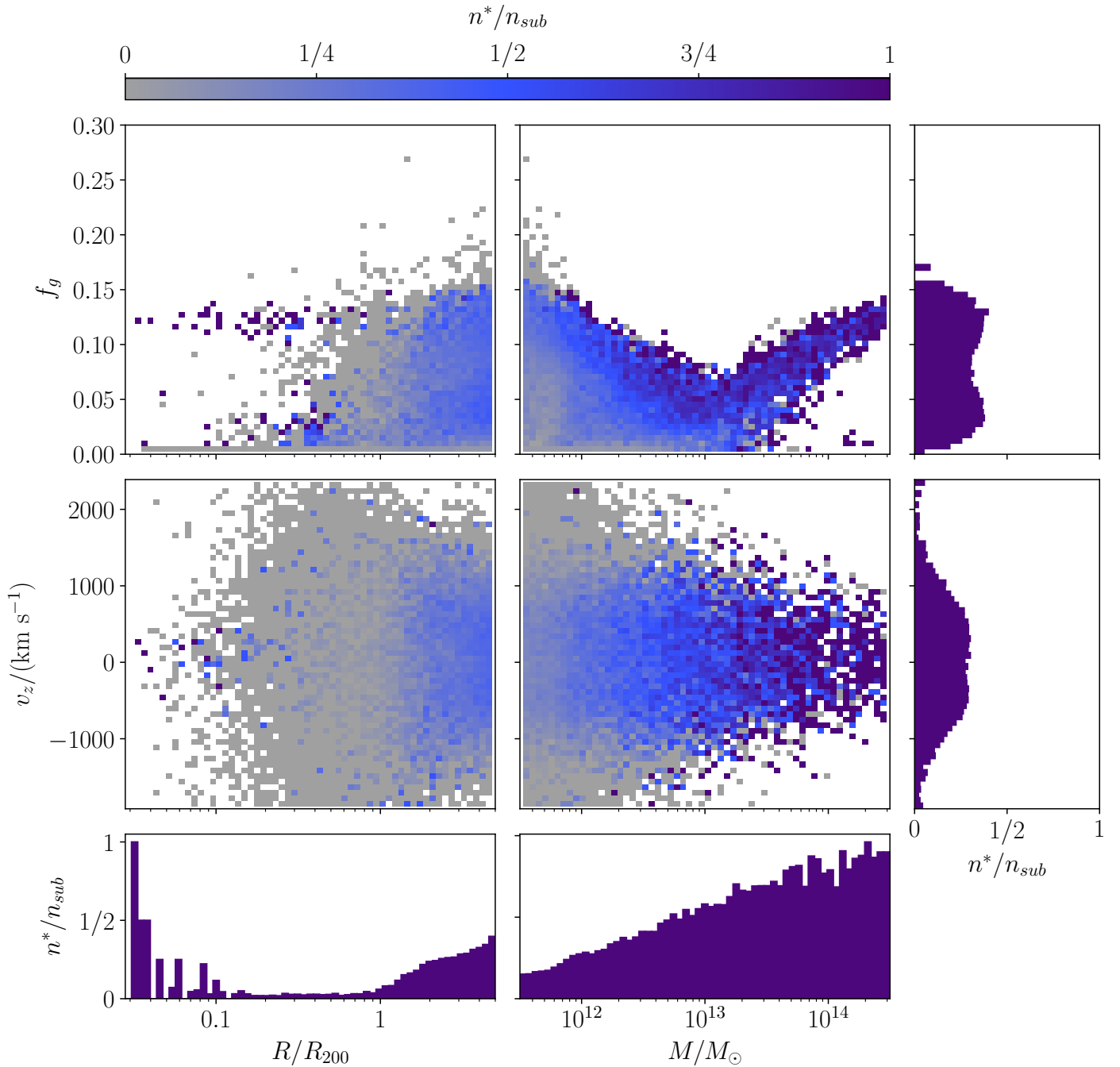
Figure 17: Probability distributions for the subhalo IGM detection, including the bulk motion of the parent clusters relative to the CMB rest frame.